

Post-failure process and kinematic behavior of two landslides: Case study and material point analyses

Thanh Son Nguyen^a, Kuo-Hsin Yang^{b,*}, Yu-Kuei Wu^b, Fuchen Teng^c, Wei-An Chao^d, Wei-Lin Lee^e

^a Faculty of Bridges and Roads, Hanoi University of Civil Engineering (HUCE), 55 Giai Phong Rd., Hai Ba Trung Dist., Hanoi, Viet Nam

^b Department of Civil Engineering, National Taiwan University (NTU), 1, Sec. 4, Roosevelt Rd., Taipei, Taiwan

^c Department of Civil and Construction Engineering, National Taiwan University of Science and Technology (Taiwan Tech), 43, Sec. 4, Keelung Rd., Taipei, Taiwan

^d Department of Civil Engineering, National Yang Ming Chiao Tung University (NYCU), 1001 University Rd., Hsinchu, Taiwan

^e Slope and Hydrology Division, National Science and Technology Center for Disaster Reduction (NCDR), 9F., No. 200, Sec. 3, Beixin Rd., New Taipei City, Taiwan

ARTICLE INFO

Keywords:

Landslide case study
Material point method
Post-failure
Kinematic behavior
Runout distance
Deposit height

ABSTRACT

This paper presents a comprehensive and well-documented landslide case study involving detailed site investigation, field tests, seismic signal analyses, and advanced numerical analyses using the material point method (MPM) to investigate the post-failure process and kinematic behavior of two landslides. The slope failures were triggered by Typhoon Jangmi in September 2008 and had impacts on the downslope residential areas. The background information of two landslides, including geological and hydrological conditions obtained from the detailed site investigation and field tests, was first introduced. The MPM analyses were then conducted and validated by comparing measured and predicted results for the final landslide profiles and duration. The numerical results, including variations in deviatoric strain, volumetric strain, and excess pore water pressure with time, were further examined to determine the post-failure mechanism of the landslides. The effects of soil drainage conditions during landslides on the final landslide profile were also compared and discussed. This study demonstrated that MPM analyses could accurately predict the runout distance of both landslides. The numerical results indicate that the landslides occurred through a complex process of soil failure that involved the stages of shearing, translational movement, compression, and deposition. When the soil was subjected to different loading conditions in different stages, the corresponding post-failure mechanisms are also different. High positive excess porewater pressure could develop near the sliding surface and has a significant influence on landslide kinematics and final landslide profiles. Compared with undrained analysis, fully coupled analysis, which permitted pore-water pressure dissipation during a landslide event, produced more accurate predictions of landslide kinematics.

1. Introduction

Landslides triggered by rainfall infiltration or phreatic surface rises are dangerous because of the high velocity of sliding soil mass, high runout distance, and high impact energy (Petley, 2012; Llano-Serna et al., 2016; Zhu et al., 2019; Guo et al., 2020). According to a global database, during 1903 to 2007, rainfall-induced landslides caused 57,028 deaths and affected more than 10 million people worldwide. In Taiwan, statistical data collected from 270 natural disaster events over a 50-year period from 1958 to 2007 (Yu et al., 2006; Harrison and Chang, 2019) revealed that 89% of landslides that occurred were related to

typhoons and heavy rainfall. In August 2009, Typhoon Morakot caused 2850 mm of precipitation over the course of approximately 100 h in Taiwan, resulting in numerous landslides and debris flows in areas of southern Taiwan (Lin et al., 2011) and more than US\$5 billion in economic losses (Tsou et al., 2011). Therefore, understanding the kinematic features of landslides, particularly for predicting landslide runout distances and deposit heights, is essential for landslide risk assessment, and landslide disaster mitigation and prevention (Bandara and Soga, 2015).

Researchers have adopted various approaches, such as field monitoring (Picarelli et al., 2005; Tu et al., 2009), experimental model testing (Moriwaki et al., 2004; Ochiai et al., 2004; Sasahara, 2017; Fan et al.,

* Corresponding author.

E-mail addresses: sonnt@huce.edu.vn (T.S. Nguyen), khyang@ntu.edu.tw (K.-H. Yang), wuk0813@gmail.com (Y.-K. Wu), fteng@mail.ntust.edu.tw (F. Teng), vnchao@nctu.edu.tw (W.-A. Chao), weilinlee@ncdr.nat.gov.tw (W.-L. Lee).

<https://doi.org/10.1016/j.compgeo.2022.104797>

Received 6 December 2021; Received in revised form 30 March 2022; Accepted 25 April 2022

0266-352X/© 2022 Elsevier Ltd. All rights reserved.

2018; Cogan and Gratchev, 2019; Chang et al., 2020; Lee et al., 2021a; Xie et al., 2020), and numerical analyses (Zhang et al., 2003; Leshchinsky et al., 2015; Li et al., 2016a; Lollino et al., 2016; Yang et al., 2017; Tang et al., 2019; Ren et al., 2020; Yang et al., 2020), to investigate landslides induced by rainfall infiltration or phreatic surface rises. These studies have primarily focused on evaluating the slope stability (i.e., factor of safety), failure mode (i.e., location of the failure surface), and failure mechanism (i.e., changes in pore water pressure [PWP] and soil effective stress) at the initiation of a landslide (i.e., landslide pre-failure and failure stages).

The capability of conventional mesh-based numerical approaches, such as the finite element method and finite difference method, to model small deformation problems has been demonstrated and is well recognized. However, these methods are generally inapplicable for modeling large nonlinear deformation problems, such as soil movement at landslide post-failure stages, because numerical illness could occur due to excessive mesh distortion and free-surface evolution during the process of solving large soil deformation problems (Chen and Qiu, 2012; Mohammadi and Taiebat, 2016; Soga et al., 2016; Yuan et al., 2020). In recent years, advanced computational algorithms have been developed to overcome mesh distortion during the process of solving large deformation problems. For example, mesh-free methods such as the smoothed particle hydrodynamics (SPH) method (Bui et al., 2008; Chen and Qiu, 2012; Huang and Dai, 2014; Nonoyama et al., 2015; Li et al., 2019; Zhang et al., 2019b; Dai et al., 2020; Mori et al., 2020; Yuan et al., 2020; Zhang et al., 2020; Liu et al., 2021), the material point method (MPM) (Andersen and Andersen, 2010; Li et al., 2016b; Llano-Serna et al., 2016; Wang et al., 2016; Yerro et al., 2016, 2019; Shi et al., 2018, 2019, 2020; Conte et al., 2019; Xu et al., 2019; Conte et al., 2020; Li et al., 2021; Troncone et al., 2019, 2020, 2022; Nguyen et al., 2021; Ying et al., 2021; Zhao et al., 2021), the discrete element method (DEM) (Li et al., 2012; Lu et al., 2014; Hung et al., 2018; Peng et al., 2019; Weng et al., 2019; Chen et al., 2020), and discontinuous deformation analysis (DDA) (Chen and Wu, 2018; Nian et al., 2020) have been applied to analyze landslides in post-failure stages. Soga et al. (2016) and Qin et al. (2022) reviewed and discussed the advantages and disadvantages of these numerical methods and reported that the MPM is one of the most favorable mesh-free techniques for modeling large deformation problems in geotechnical engineering.

Several studies in the literature have performed MPM analyses to simulate landslides in post-failure stages (Andersen and Andersen, 2010; Li et al., 2016b; Llano-Serna et al., 2016; Wang et al., 2016; Yerro et al., 2016, 2019; Shi et al., 2018, 2019, 2020; Conte et al., 2019; Xu et al., 2019; Conte et al., 2020; Li et al., 2021; Troncone et al., 2019, 2020, 2022; Nguyen et al., 2021; Ying et al., 2021). These studies have mainly investigated the influence of soil parameters and groundwater level on the final configuration and runout distance of a landslide. By comparing between predicted results and field observations of the final configuration and runout distance, the aforementioned studies have confirmed that the MPM can simulate the actual soil movement characteristics of landslides in post-failure stages. Moreover, advanced MPM formulations (i.e., multi-phase or two-layer material points) have been developed in recent years to simulate the soil-water interaction in unsaturated soil slope (Bandara et al., 2016; Wang et al., 2018; Liu et al., 2020; Ceccato et al., 2021; Cuomo et al., 2021; Feng et al., 2021; Girardi et al., 2021; Lee et al., 2021b; Liu and Wang, 2021; Yerro et al., 2022). Although considerable efforts have been made to attain updated knowledge on the soil movement characteristics of landslides, only a few studies in the literature assessed the post-failure of real landslide cases. Besides, except for the recent studies using advanced MPM formulations to simulate the rainfall infiltration, many past studies neglected the effect of the excess PWP in the analyses to reduce the computational time. They simulated soil as a dry material using total stress analysis or assumed saturated soil with high hydraulic conductivity under drained conditions so negligible excess PWP was generated and could be dissipated rapidly. The development of excess PWP during landslides and how it influences the

kinematic behavior of landslides have not been fully investigated and reported in the literature. Moreover, past studies in the literature only consider one single type of analysis (i.e., undrained, drained, and coupled analyses) to simulate landslide. No study evaluates and compares the influence of different analysis types on predicting the final landslide profile.

This paper presents a comprehensive and well-documented landslide case study involving detailed site investigation, field tests, seismic signal analyses, and advanced numerical analyses using the material point method to investigate the post-failure process and kinematic behavior of two landslides. The specific objectives of this study were to 1) present a comprehensive and well-documented landslide case study involving both detailed experimental and numerical studies; 2) validate the suitability and applicability of the MPM for analyzing landslides in post-failure stages; 3) investigate the post-failure process and kinematic behavior of two landslides; 4) examine the post-failure mechanism of landslides, especially for the development of excess PWP during landslides and how it influences the kinematic behavior of landslides; and 5) evaluate the influence of different analysis types on predicting the final landslide profile. In this study, the background information of two landslides, including geological and hydrological conditions obtained from the detailed site investigation and field tests, was first introduced. The numerical analyses were then conducted and rigorously validated by comparing measured and predicted results for the final landslide profiles and duration. After the model validation, the post-failure process and kinematic behavior of the landslides (i.e., landslide displacement, velocity, runout distance, and deposit height) were discussed, and their post-failure mechanism (i.e., variations in deviatoric strain, volumetric strain, and excess PWP with time) was further examined. Moreover, because of an elapse of only a few seconds between the beginning and end of a landslide, the possibility of modeling soil during a landslide under undrained conditions was explored. Two types of analyses (i.e., undrained-effective stress analysis and fully coupled hydro-mechanical analysis) were performed to model soil behavior during landslides under undrained and drained conditions. The influence of soil drainage conditions on the final landslide profile was examined. The results of this study would provide insights into the landslide process as well as useful information for landslide risk assessment, and landslide disaster mitigation and prevention.

2. Fundamentals of MPM analysis

2.1. Features of the MPM

The Anura3D code developed by the Anura3D MPM Research Community (Anura3D_v2019) was employed for the MPM analyses in this study. The primary feature of the MPM is that the continuum medium is represented as a combination of material points (MPs) (i.e., Lagrangian particles) and background mesh (i.e., Eulerian grids). The material (i.e., soil or water) is divided into discrete MPs that can freely move in the defined problem domain based on the Lagrangian description of the media. The MPs carry and transmit all of the physical information of the continuum medium (e.g., velocities, strains, stresses, and state variables). This enables models to be incorporated with advanced constitutive materials as history-dependent variables that are tracked through simulation. The physical properties of the MPs are then transferred to the background mesh. An incremental scheme is applied at each time step to solve the governing equations at the nodes of the background mesh. The merits of the Lagrangian particles and Eulerian grids are integrated to prevent interference from convection terms or mesh distortion during the process of solving large deformation problems (Soga et al., 2016). This section introduces the basic governing equations and computation cycle of MPM analysis. A detailed description of the theory, formulations, time discretization, and solution algorithms of MPM analyses can be found in the book by Fern et al. (2019).

2.2. Governing equations

In this study, a fully coupled hydro-mechanical analysis with a single two-phase (solid and liquid phases) MP was used to simulate the changes in PWP during landslides (i.e., partially drained condition of saturated soil). This section introduces formulations for the coupled dynamic, two-phase problem proposed by Fern et al. (2019). In a defined problem domain, the continuum can be described by a set of differential governing equations, including the mass and momentum conservation of each phase and the mixture (i.e., saturated soil).

The mass conservation of the solid phase is expressed as follows:

$$\frac{d}{dt}[(1-n)\rho_s] + (1-n)\rho_s \nabla \cdot \mathbf{v}_s = 0 \tag{1}$$

where n is the porosity, ρ_s is the density of solid skeleton, $\mathbf{v}_s = \mathbf{v}_s(\mathbf{x}, t)$ is the velocity vector of solid, $\nabla \cdot \mathbf{v}_s$ represents the divergence of the vector field \mathbf{v}_s , and \mathbf{x} and t indicate the spatial coordinates and time. The mass conservation of the liquid phase is written as follows:

$$\frac{d(n\rho_L)}{dt} + n\rho_L \nabla \cdot \mathbf{v}_L = 0 \tag{2}$$

where ρ_L is the density of liquid, and $\mathbf{v}_L = \mathbf{v}_L(\mathbf{x}, t)$ is the velocity vector of liquid. From combining Eqs. (1) and (2) under the assumption of the

presence of incompressible solid grains and no spatial variations in densities and porosity, the mass conservation of the saturated soil, also known as the storage equation, can be obtained as follows:

$$\frac{d\varepsilon_{v,L}}{dt} = \frac{1}{n} [(1-n) \nabla \cdot \mathbf{v}_s + n \nabla \cdot \mathbf{v}_L] \tag{3}$$

where $\varepsilon_{v,L}$ is the effective volumetric strain in the liquid.

The momentum conservation of the solid phase is expressed as:

$$(1-n)\rho_s \frac{d\mathbf{v}_s}{dt} - \nabla \cdot \boldsymbol{\sigma}' - (1-n)\nabla u - (1-n)\rho_s \mathbf{g} - \frac{n^2 \rho_L \mathbf{g}}{k} (\mathbf{v}_L - \mathbf{v}_s) = 0 \tag{4}$$

where $\boldsymbol{\sigma}'$ is the Cauchy effective stress tensor, u is the PWP, \mathbf{g} is the gravitational acceleration vector, k is the soil hydraulic conductivity based on Darcy's Law, and $\mathbf{v}_L - \mathbf{v}_s$ represents the relative velocity of the liquid respect to the solid. The last item in Eq. (4) denotes the drag force, which represents the interaction force between the solid and liquid phases. The momentum conservation of the liquid phase can be expressed as follows:

$$n\rho_L \frac{d\mathbf{v}_L}{dt} - n\nabla u - n\rho_L \mathbf{g} + \frac{n^2 \rho_L \mathbf{g}}{k} (\mathbf{v}_L - \mathbf{v}_s) = 0 \tag{5}$$

The momentum conservation of the saturated soil can be obtained

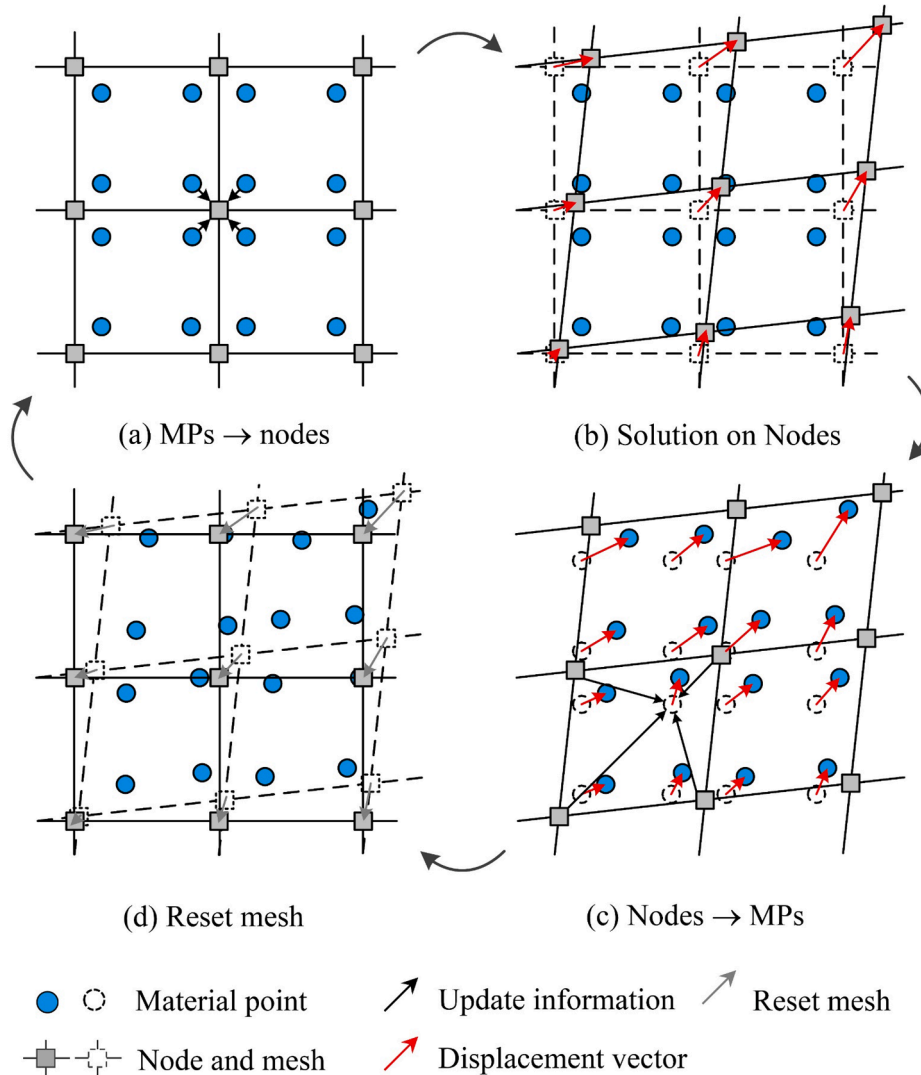


Fig. 1. Computational cycle of MPM: (a) map MP information to nodes; (b) solve equilibrium equations on nodes and update nodal information and positions; (c) map nodal information to MPs and update MPs' information and positions; (d) reset mesh.

from combining Eqs. (4) and (5) as follows:

$$(1 - n)\rho_S \frac{dv_S}{dt} + n\rho_L \frac{dv_L}{dt} = \nabla \cdot \sigma + \rho g \quad (6)$$

where σ is the Cauchy total stress tensor, and $\rho = [(1 - n)\rho_S + n\rho_L]$ is the density of saturated soil. In summary, the two-phase problem is described by the mass conservation equation for saturated soil (Eq. (3)), two momentum conservation equations (Eq. (5) for the liquid phase and Eq. (6) for saturated soil), and constitutive equation for the soil skeleton. Because the MPs carry the mass, the mass conservation equation is satisfied within the defined problem domain. The two momentum conservation equations are transformed into weak forms, discretized into finite elements and nodes through the use of interpolation functions, and solved for soil skeleton acceleration and pore liquid acceleration as the primary unknown variables.

2.3. Computational cycle and procedure

Fig. 1 presents the standard MPM procedure for one computational cycle (i.e., one time step). In the first step of the cycle (Fig. 1a), all of the physical information is mapped from the MPs to the nodes in the background mesh through interpolation functions (i.e., shape functions). In the second step (Fig. 1b), boundary conditions can be imposed at the nodes in the background mesh or at the MPs, and the explicit dynamic computation scheme is employed to solve the governing equations. The momentum conservation equations (Eqs. (5) and (6)) are solved to obtain the nodal acceleration values as the primary unknown variables. In the third step (Fig. 1c), these nodal values are then used to update the acceleration, velocity, and position of the MPs as well as to compute the strains and stresses at the MPs. Moreover, the density and volume of the MPs can be updated according to the increment in volumetric strain. In the final step (Fig. 1d), because the physical information associated with the mesh is transferred to the MPs, each MP is assigned updated values for mass, velocity, acceleration, stress, strain, and other

relevant properties characterizing the state of the material. No permanent information is required to be stored in the background mesh at the end of the computational cycle. The deformed mesh can subsequently be reset to avoid the problem of excessive mesh distortion. The reset mesh is then ready for the next computational cycle of the analysis.

3. Case histories and site conditions

3.1. Description of two landslides

Two landslides that occurred at Jintou Mountain in the southern area of Taipei Basin were studied (Fig. 2). Fig. 3 displays the slope topography, landslide area, and borehole locations of the investigated landslides. These two landslides occurred in close proximity (less than 1 km apart) and were caused by torrential rainfall during Typhoon Jangmi on September 26–28, 2008.

The first landslide area (hereafter referred to as Slope 1) was located downhill of the No. 16 support tower of the Taipei Maokong Gondola system (Fig. 2a). The average slope angle of Slope 1 before the landslide was $\beta = 26^\circ$. During the landslide, Slope 1 slid northwestward. The landslide area had a length of approximately 230 m and a width of 20–80 m and was located at an elevation of 150–280 m above sea level. The landslide area was 11,700 m², and the total volume of the landslide mass was estimated to be 23,700 m³ (Yang et al., 2017). A field investigation revealed that the landslide occurred in residual soil and the highly weathered/fractured rock layer. The landslide affected a residential community downhill. A large amount of landslide mass was deposited in a playground area of this residential community. The collapsed slope also exposed the pile foundation of the Gondola tower uphill. Operation of the Maokong Gondola was suspended for 16 months due to concerns regarding potential damage to the foundation of the gondola pylons. Thereafter, massive geotechnical investigation, instrumentation, and remediation programs were implemented to ensure the stability of the adjacent slopes and safety of the gondola system.

The second landslide area (hereafter referred to as Slope 2) was

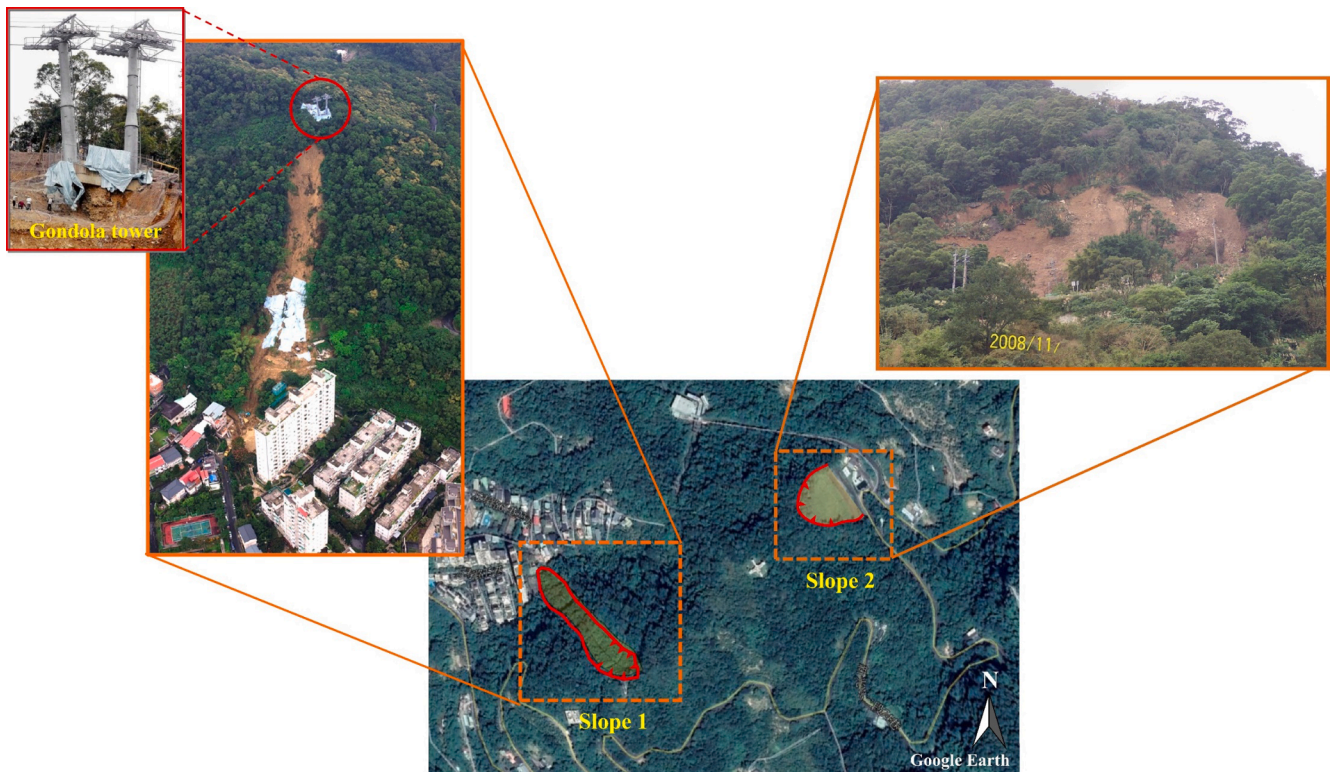


Fig. 2. Aerial view and photos of two landslide cases.

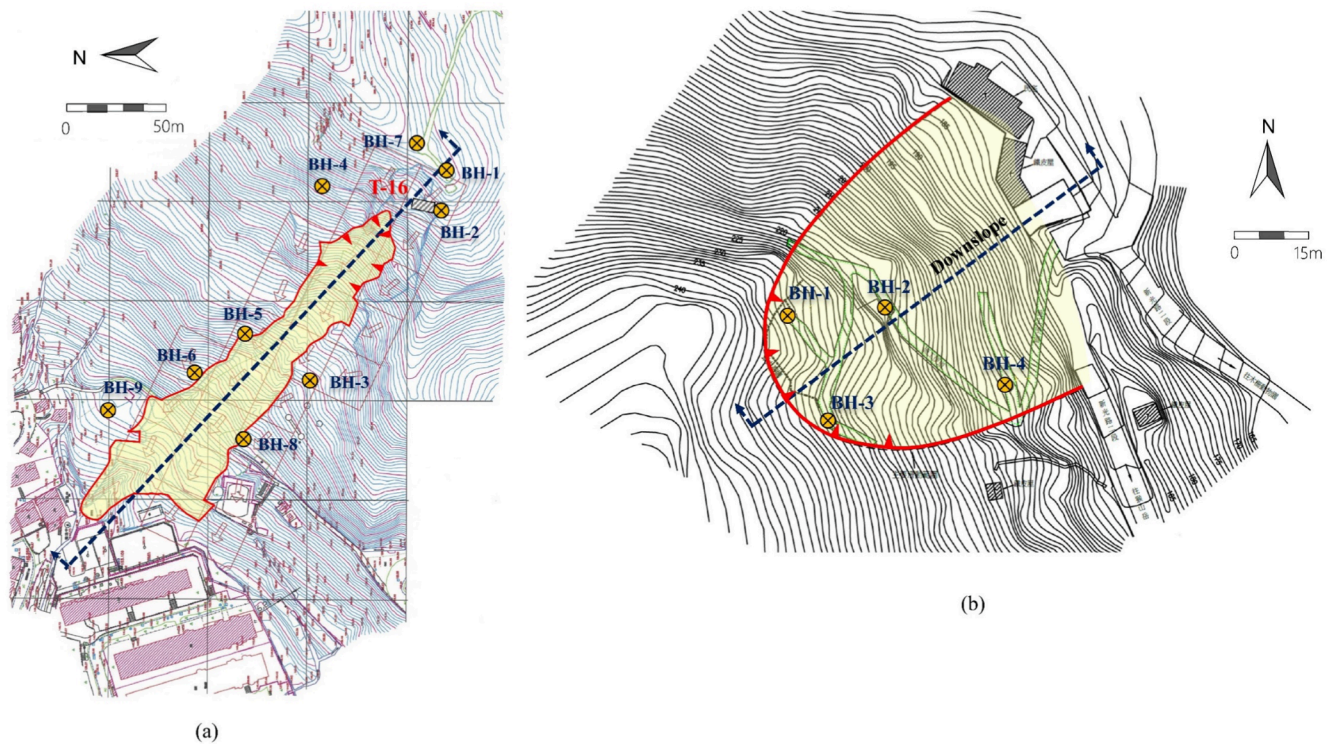


Fig. 3. Slope topography, landslide areas and borehole locations: (a) Slope 1; (b) Slope 2.

located uphill of a local access road to a chicken farm and the farmer's house (Fig. 2b). The average slope angles of Slope 2 before the landslide were $\beta = 22^\circ$ and 36° at the upper and lower parts of the slope, respectively. Slope 2 slid northeastward. The landslide had a length of approximately 100–150 m and a width of 100–120 m and was located at an elevation of 140–240 m above sea level. The landslide area was approximately of 10,000–20,000 m² (Lin et al., 2019). A field investigation revealed that the landslide occurred in residual soil and the highly weathered/fractured rock layer. The landslide mass blocked the access road and buried the chicken shed of the chicken farm. Fortunately, the farmer's house, located only 15 m in front of the chicken shed, was unaffected by the landslide.

Numerical analyses had previously been performed to investigate the failure mechanisms and hydraulic responses of the two slopes. For Slope 1, Yang et al. (2017) performed fully coupled hydro-mechanical FE analyses based on a mechanical framework for unsaturated soil. The numerical results indicated that the failure of Slope 1 began in the shallow region of the slope (at a depth of 2 m from the slope surface). The failure mechanism was attributed to the advancement of the wetting front induced by rainfall infiltration. As the rainfall infiltrated, the surface soil became fully saturated. The PWP of the residual soil changed from negative to positive, causing suction loss, leading to a decrease in soil shear strength and finally resulting in slope instability. For Slope 2, Lin et al. (2019) first performed transient seepage analyses to determine the PWP distribution within the slope, and the computed PWP was then integrated into slope stability analyses to evaluate the factor of safety of the slope. The numerical results revealed that the initial failure point was located at the toe of the residual soil, and the failure was caused by the accumulation of positive PWP up to 20 kPa (i.e., increase in the groundwater level) in this area. These studies only explained the failure mechanisms at the onset of slope failure. Because of limitations of the numerical methods they used, the post-failure process and kinematic behavior of these landslides were not investigated.

3.2. Geological and hydrological conditions

Information on subsurface soil and groundwater along the inspected slopes was obtained from in situ and laboratory tests conducted during a site investigation program. Fig. 3 displays the locations of boreholes in the two slopes, and Fig. 4 shows a typical borehole log of soil and rock samples. Fig. 5 depicts a cross-section of the slope geometry and geological profiles of the two slopes. The surface layer of the slopes is composed of residual soil and a highly weathered/fractured rock layer with a depth from 2 to 10 m. The residual soil, decomposed from underlain weathered sandstone and shale, consists of silty sand (SP), low-plastic silt, (ML) and limited low-plastic clay (CL with plasticity index $PI = 10$ –15). The SPT values of the residual soil in the two slopes range from $N_{60} = 12$ to 35, with a mean of 21. The Miocene Taliao formation and Shihti formation form the slope bedrock, which consists of sandstone (SS), shale (SH), sandstone-shale interbedded (SS-SH), and shale with few sandstone (SH/ss). The attitude (strike/dip angle) of the bedrock layers of the two investigated slopes is $N50^\circ$ – $60^\circ E/10^\circ$ – $20^\circ SE$ for Slope 1 and $N65^\circ E/20^\circ$ – $30^\circ S$ for Slope 2; accordingly, Slope 1 can be classified as an anacinal slope and Slope 2 as an orthoclinal slope.

The groundwater level (GWL) under normal conditions was measured at the locations of various boreholes (Fig. 5); it was 8 to 12 m below the slope surface for Slope 1 and was below the residual soil (25 to 45 m) for Slope 2. Fig. 6 presents a histogram of the hourly rainfall during Typhoon Jangmi, which caused a total precipitation of 450 mm in 3 days in that region. The landslides occurred 50 and 32 h after the beginning of the typhoon event, and the corresponding cumulative rainfall at the time that the landslides were triggered was 400 and 134 mm for Slope 1 and Slope 2, respectively. Changes in GWL during Typhoon Jangmi were not monitored. As discussed, the numerical results of Lin et al. (2019) and Yang et al. (2017) indicate that some parts of the soil in the slopes may have become fully saturated and developed a positive PWP during the typhoon event.

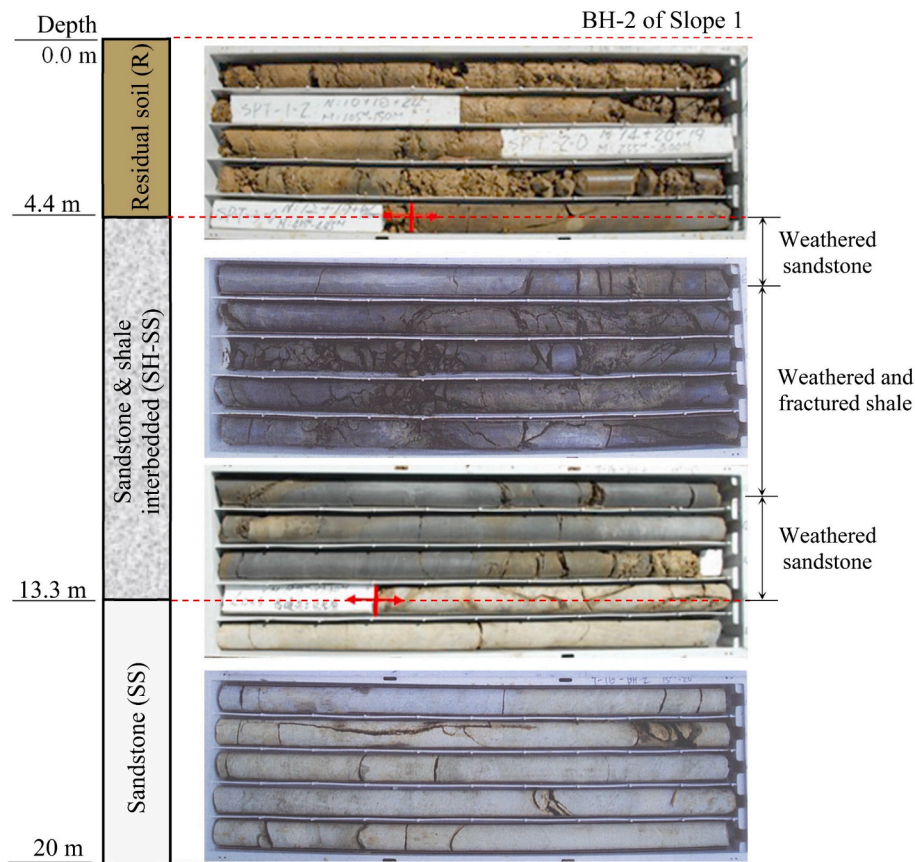


Fig. 4. Typical borehole log of soil and rock samples.

4. Numerical simulation

4.1. Numerical modeling and simulation procedure

Fig. 7 presents the MPM models and tracking points of the two slopes. A three-node linear triangular element with 3 MPs was designed for the soil element. In total, the numerical model consisted of 4011 and 5125 elements, 2133 and 2678 nodes, and 5190 and 4869 MPs for Slope 1 and Slope 2, respectively. The number of MPs was selected on the basis of the relationship between the model height and number of MPs as suggested by Llano-Serna et al. (2016). The element sizes were refined in the residual soil layer where the shear failure surface was expected to develop. To reduce the computation time, the bedrock layer was considered to have an average thickness of only 10 m in the numerical model. In Fig. 7, the tracking points D were distributed at the surface of the slope and were used to monitor variations in the displacement and velocity of the sliding soil mass. The tracking points P were assigned to the bottom of the residual soil to investigate the changes in soil volumetric strain and excess PWP during the landslides.

Fig. 7 also illustrates the boundary conditions. Standard settings were applied for the boundary conditions for both the solid and liquid phases; the bottom of the bedrock layer was fully fixed, and the horizontal movement of the left and right boundaries was restricted. Examination of the developed stress and displacement levels in the numerical models revealed that the assumed boundary conditions were appropriate.

The simulation procedure comprised two sequential steps: (1) simulation of gravity loading and (2) simulation of the kinematic process of the landslide. In the first stage, the gravity load was activated to generate in situ stress, and the model was heavily damped to prevent the occurrence of large displacement during the first stage of the calculation process. According to the recommendations in the Anura3D user

manual, an overall local damping coefficient of 75% was imposed for all active elements to accelerate the numerical convergence to quasi-static equilibrium. In the second stage, the landslide was allowed to proceed, and the landslide progress was simulated. The overall local damping coefficient was reduced to 5%, which a typical value suggested by Yerro et al. (2019), to prevent the system from becoming overly damped during dynamic computation, which could result in high energy dissipation and could therefore influence the accuracy of predictions of the kinematic behavior of landslides. Moreover, because explicit dynamic formulations were used to calculate the solutions, the calculation time was discretized into small time steps. Each time step was set at 1×10^{-4} s to ensure the stability and accuracy of the analyses. The simulation was terminated when landslide movement stopped, specifically when the velocity of the sliding soil mass reached to zero.

4.2. Input material properties

Table 1 summarizes the material properties adopted in the present study and types of analysis performed. Residual soil was simulated using the Mohr–Coulomb model with effective stress properties. Fully coupled hydro-mechanical analysis with a single two-phase MP was assigned to the residual soil to simulate changes in PWP during the landslides. The residual soil was assumed to be saturated, but the soil cohesion values were modified to account for the effect of apparent cohesion under partially saturated conditions in the field. The effective stress soil shear strength properties of the two slopes were determined through direct shear tests performed on undisturbed soil samples obtained during the site investigation program. Regarding the soil shear strength properties, the effective cohesion c' was in the range of 5–15 kPa, and the effective friction angle ϕ' was in the range of 24°–28°. The values $c' = 6$ kPa and $\phi' = 27^\circ$ were selected in the present study. The same soil input values were also used by Lin et al. (2019) and Yang et al. (2017).

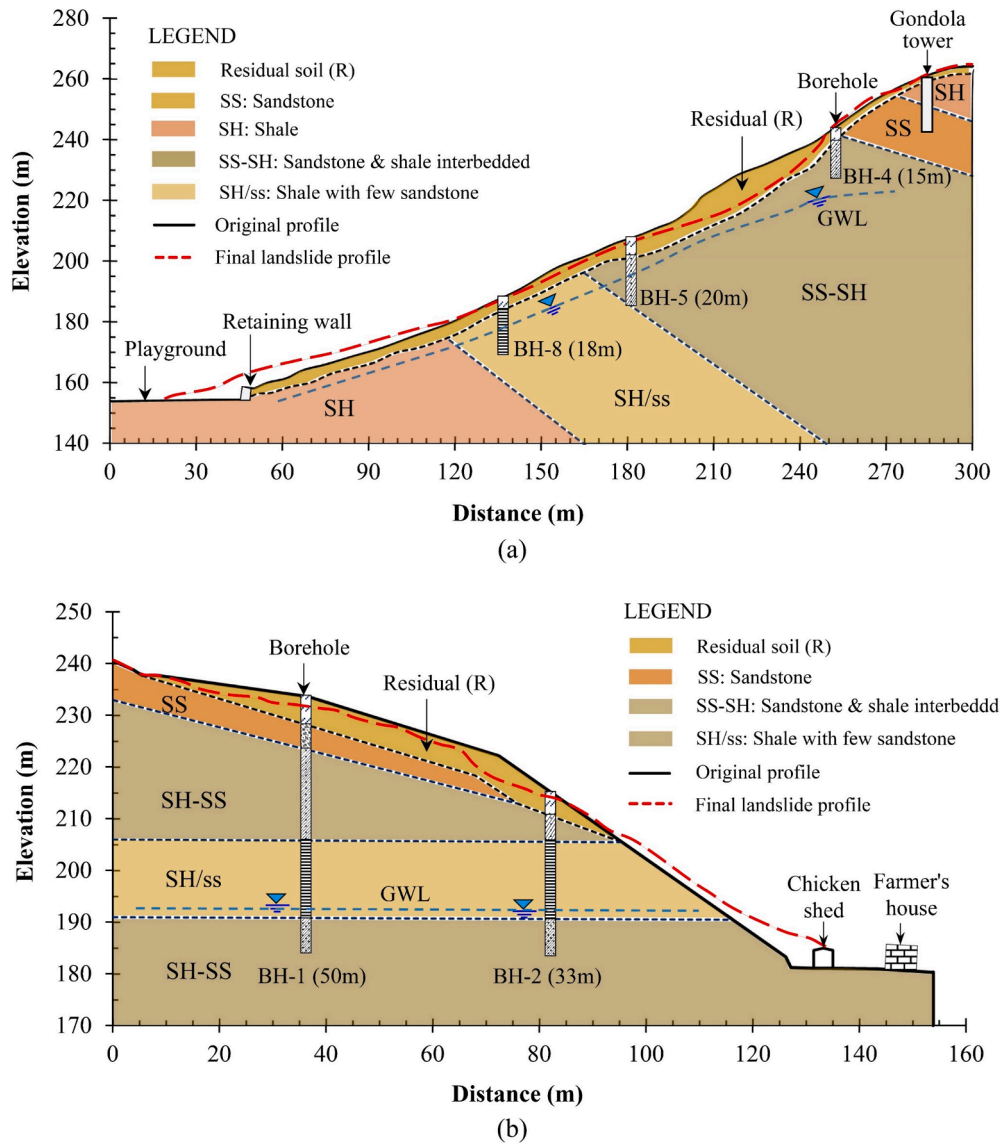


Fig. 5. Cross-section of the slope geometry and geological profiles: (a) Slope 1; (b) Slope 2.

To account for partially saturated conditions in the field, the extended Mohr–Coulomb failure criterion proposed by Vanapalli et al. (1996) was adopted to model the nonlinear relationship between unsaturated soil shear strength and matric suction, which can be expressed as follows:

$$\tau = c' + \Theta(u_a - u_w)\tan\phi' + (\sigma - u_a)\tan\phi' \quad (7)$$

where τ is the soil shear strength, c' and ϕ' are the effective cohesion and friction angle, σ is the normal stress, $(u_a - u_w)$ is the matric suction (where u_a and u_w are the pore air and PWP, respectively), Θ is the normalized volumetric water content, expressed as:

$$\Theta = \frac{\theta - \theta_r}{\theta_s - \theta_r} \quad (8)$$

where θ is the field volumetric water content, θ_s is the saturated volumetric water content, θ_r is the residual volumetric water content. The right side of Eq. (7) represents the soil shear strength from soil cohesion, matric suction, and soil friction. The second term of Eq. (7) can be view as an apparent cohesion c_a induced by matric suction under unsaturated soil conditions. The expression for c_a can be obtained from substituting Eq. (8) into the second term of Eq. (7):

$$c_a = \left(\frac{\theta - \theta_r}{\theta_s - \theta_r} \right) (u_a - u_w) \tan\phi' \quad (9)$$

According to the soil water characteristics of the residual soil and the average matric suction value (≈ 25 kPa) during slope failure reported by Lin et al. (2019) and Yang et al. (2017), the c_a values of 4 and 2 kPa were obtained for Slope 1 and Slope 2, respectively. Combining c_a and c' yielded total cohesion of the residual soil c values of 10 and 8 kPa, which were used in the analyses (Table 1).

The soil modulus of the residual soil was estimated on the basis of empirical correlations. The initial soil modulus E_i of the residual soil was first estimated with the empirical equation proposed by Schmertmann (1970) and Kulhawy and Mayne (1990), which is expressed as follows:

$$E_i = \alpha_f p_a N_{60} \quad (10)$$

where α_f is the coefficient to account for fine content (=5 was applied for sands with fines); p_a is one atmospheric pressure (=101.3 kPa); and N_{60} is the corrected SPT-N value (the mean SPT value $N_{60} = 21$ is used to represent the average soil conditions). E_i in Eq. (10) was then converted into the soil modulus at 50% of the stress level E_{50} on the basis of the assumption that the soil stress–strain relation takes the form of a

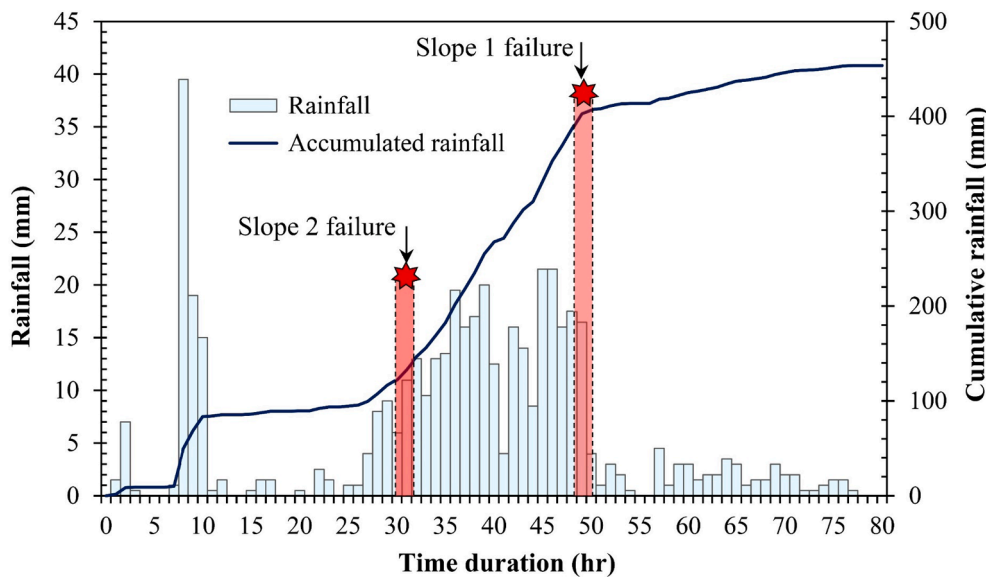


Fig. 6. Rainfall histogram and cumulative rainfall during Typhoon Jangmi.

hyperbolic curve.

$$E_{50} = E_i \frac{2 - R_f}{2} \quad (11)$$

where R_f is the failure ratio (a typical value of 0.9 was used). The E_{50} corresponds to the Young's modulus E in Mohr-Coulomb model used in this study. As shown in Table 1, the E value calculated with Eqs. (10) and (11) was 5651 kPa.

The saturated soil hydraulic conductivity k_s was determined to be 2.76×10^{-6} m/s from a field permeability test conducted at a depth of 0.1–0.5 m using a portable Guelph permeameter (Yang et al., 2017). The effect of soil dilatancy was not considered in the simulation because the residual soil had been decomposed from the weathered bedrock and loosely deposited in the field. Additionally, because no information had been reported regarding the soil–rock interface friction coefficient, the frictional contact (or interface element) between the soil layer and bedrock was not included in the simulations.

The bedrock was simulated using the Mohr–Coulomb model with total stress properties. Undrained analysis was assigned to the bedrock because of its relatively low permeability. The undrained shear strength s_u of the bedrock layer was obtained from the average of the measured uniaxial compression strength of the rock samples. The Young's modulus and saturated hydraulic conductivity of the bedrock layer were estimated according to the properties of similar rock types, as suggested by Goodman (1989). The structures, including the retaining wall in Slope 1 and chicken shed in Slope 2, were modeled as linear elastic materials under dry conditions (the effect of PWP was not considered). The input properties of the structures were adopted from the typical properties of reinforced concrete.

5. Results and discussion

5.1. Results for Slope 1

5.1.1. Comparison for final landslide profile

Fig. 8 presents a comparison of the final landslide profiles obtained from field observations and numerical predictions. The field measurements were obtained through a total station survey supplemented with the seismic refraction method for geophysical exploration to determine the residual soil thickness at several locations along the slope. Table 2 summarizes the results for the runout distance and deposit height from the field observations and numerical analyses. As indicated in Fig. 8a,

the runout distance was defined as the distance from the toe of the residual soil of the original slope to the forefront of the final slope configuration. The deposit height was the maximum height of the landslide deposit. Overall, the predicted final landslide profile matched well with the measured profile. In the landslide deposition area, the predicted runout distance (29.8 m) was close to the measured distance (26.9 m), but the predicted deposit height (11.4 m) was higher than the measured height (8.2 m) (Table 2). The actual landslide mass dispersed across the playground area and exhibited a fan-shaped deposit that was affected by the three-dimensional topographic characteristics of the field. However, this three-dimensional fan-shaped deposit as the lateral extension of the slide mass could not be simulated due to the limitations of the two-dimensional analysis methods employed in this study. This finding is supported by Yerro et al. (2019).

5.1.2. Post-failure process and kinematic behavior

Fig. 9a depicts the development and distribution of the soil deviatoric strain of Slope 1 at different time points for the evaluation of the shear failure surface during the landslide. The landslide duration from initiation to completion was 18 s, which is consistent with the results of seismic signal analyses conducted on the basis of local seismic records (Fig. 10). Using seismic records from the BATS stations (Broadband Array in Taiwan for Seismology; <https://bats.earth.sinica.edu.tw>), landslide events could be successfully detected by the geohazard location approach (Chen et al., 2013; Chang et al., 2021). This study identified that the event size is estimated to be a seismic magnitude of 2.3. With available seismic signals recorded at station SLBB (an epicenter distance of 26 km), a signal duration of 15 s was observed and can be an indicator for landslide source duration (Fig. 10). The slightly shorter landslide duration determined from seismic signal analyses is probably because the seismic motion sensors may not register the landslide movement with a low velocity at the onset and near the end of landslide.

Overall, the soil failed progressively from the upper to lower slope. At $t = 1$ s, the shear failure surface began to develop at the soil–bedrock interface of the upper slope. At $t = 3$ s, the displacement of the residual soil at the upper slope could be clearly observed and appeared to exhibit a rotational movement. At $t = 6$ s, the sliding soil mass, which originated from failure at the upper slope, moved downhill as a result of gravity and inertial force. The landslide movement became translational due to topographic constraints (i.e., a shallow residual soil layer) in the middle slope. The shear failure surface developed along the soil–bedrock interface. The deviatoric strain gradually increased from the top to

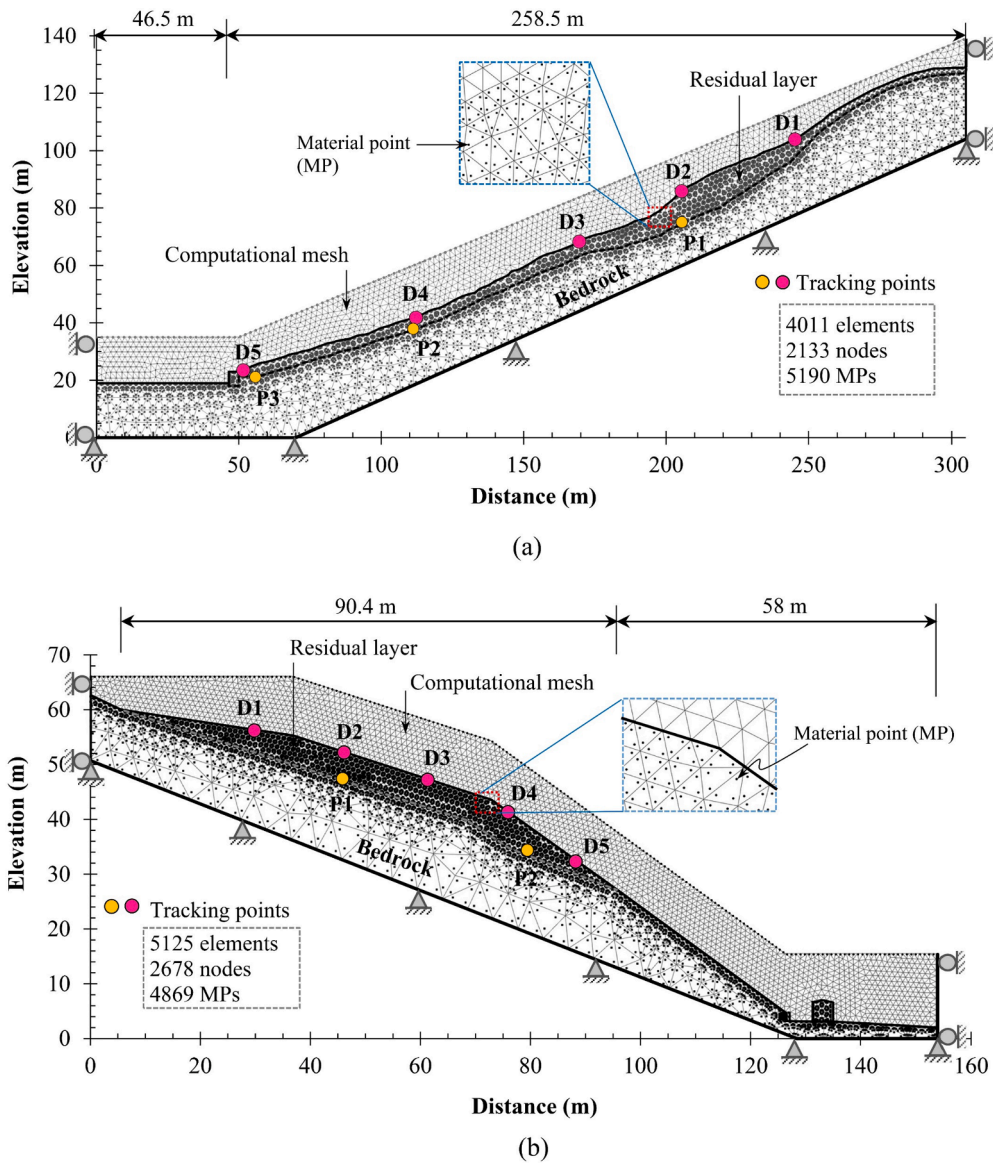


Fig. 7. MPM models and tracking points used in simulation: (a) Slope 1; (b) Slope 2.

Table 1
Input material properties used for numerical analyses.

Parameters	Symbol	Residual soil (R)		Bedrock	Structures
		Slope 1	Slope 2		
Constitutive model		Mohr-Coulomb	Mohr-Coulomb	Mohr-Coulomb	Linear Elasticity
Type of analysis		Saturated-fully coupled	Saturated-fully coupled	Saturated-Undrained	Dry
Porosity	n	0.38	0.38	0.1	0.1
Unit weight (kN/m ³)	γ	20.1	20.1	25.4	24
Cohesion (kPa)	c or s_u	10	8	4680	–
Friction angle (°)	ϕ'	27	27	0	–
Dilatancy angle (°)	ψ	0	0	0	–
Young's modulus (kPa)	E	5651	5651	1.14×10^6	5×10^5
Poisson's ratio	ν	0.3	0.3	0.495	0.17
Saturated permeability (m/s)	k_s	2.76×10^{-6}	2.76×10^{-6}	2×10^{-10}	–

Note: 1. The cohesion of the residual soil is the combination of soil effective cohesion and apparent cohesion to account for the partially saturated conditions in the field.

2. The structure indicates the retaining wall in Slope 1, and the chicken shed in Slope 2.

bottom of the sliding soil mass, indicating that the motion of large portions of the soil was laminar without considerable internal deformation or significant interlayer mixing during the translational

movement. The soil strata remained largely unchanged and were preserved in the initial order. Substantial internal deformation of the soil was inhibited because the shearing process occurred within a short time

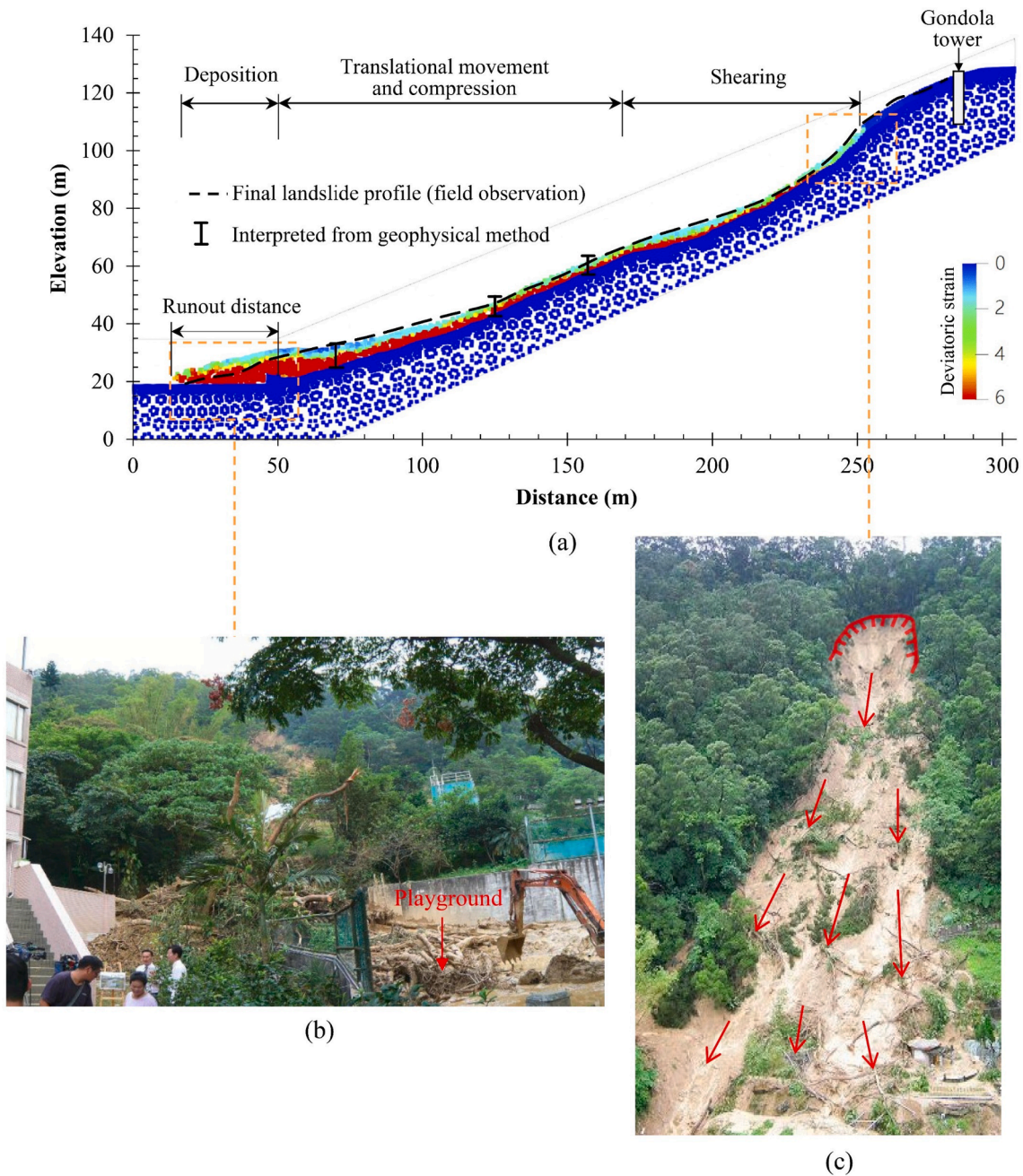


Fig. 8. Model validation: (a) comparison of final landslide profile of Slope 1; (b) photo of soil deposition at playground area; (c) photo of landslide scarp.

Table 2
Summary of the results of field observation and numerical analyses.

Type of analysis	Slope 1			Slope 2		
	Field observation	Fully coupled analysis	Undrained analysis	Field observation	Fully coupled analysis	Undrained analysis
Runout distance (m)	26.9	29.8 (+10.8%)	21.4 (-20.5%)	38	37.8 (+0.5%)	35.4 (-6.8%)
Deposit height (m)	8.2	11.4 (+39.0%)	10.9 (+32.9%)	7.0	7.2 (+4.7%)	4.7 (-32.9%)
Computational time (hr)	-	143	0.8	-	90	0.5

Note: the values in the parentheses () indicate the relative error with respect to the field observation.

frame (Li et al., 2016). At $t = 12$ s, the sliding soil mass reached the lower slope. The soil in this area was compressed and pushed passively downward. The development of the shear failure surface extended from

the soil–bedrock interface to the surface of the sliding soil mass. In the final stage ($t = 14$ – 18 s), the sliding soil mass reached the playground area and continued moving forward. Finally, the sliding soil mass

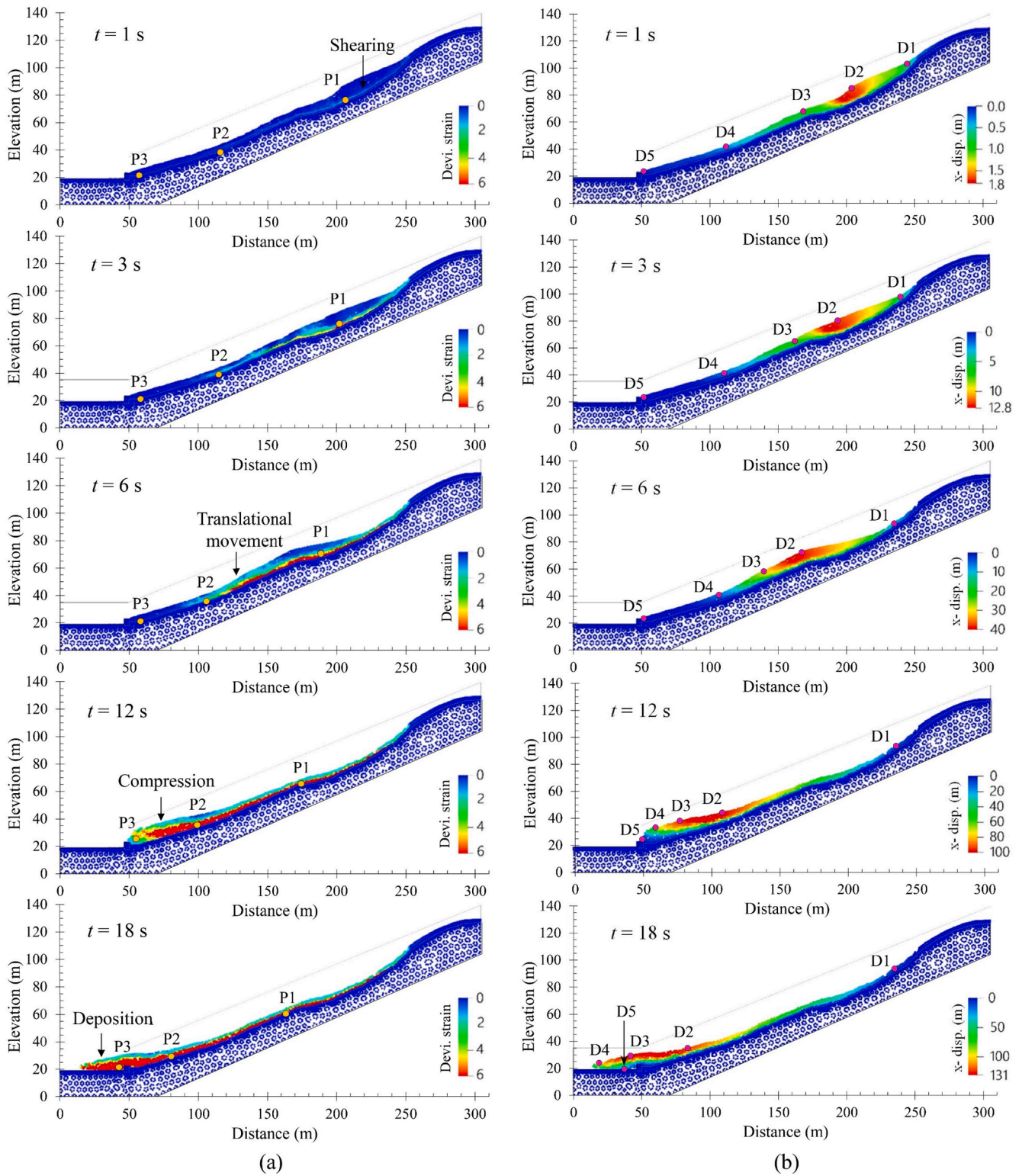


Fig. 9. Post-failure process of Slope 1 at different times: (a) deviatoric strain; (b) horizontal displacement.

completely stopped moving and was deposited over the playground area when the kinetic energy had fully dissipated through friction and shear deformation.

Fig. 9b presents a plot of the soil horizontal displacement of Slope 1 at different time points. The tracking points, as indicated in Fig. 7a and Fig. 9b, were located at the surface of the slope where the largest displacement occurred. Fig. 11 displays variations in displacement and

velocity with time that were obtained at the three selected tracking points (D2, D4, and D5 in the upper, middle, and lower slope, respectively). The soil at D1, located near the landslide scarp, traveled the shortest distance, with a displacement of only approximately 10 m, and stopped sliding at approximately $t = 5$ s. The soil at D2 and D3 at the upper and middle slope, respectively, exhibited the greatest displacement, with a travel distance of approximately 125 m. The soil at D4,

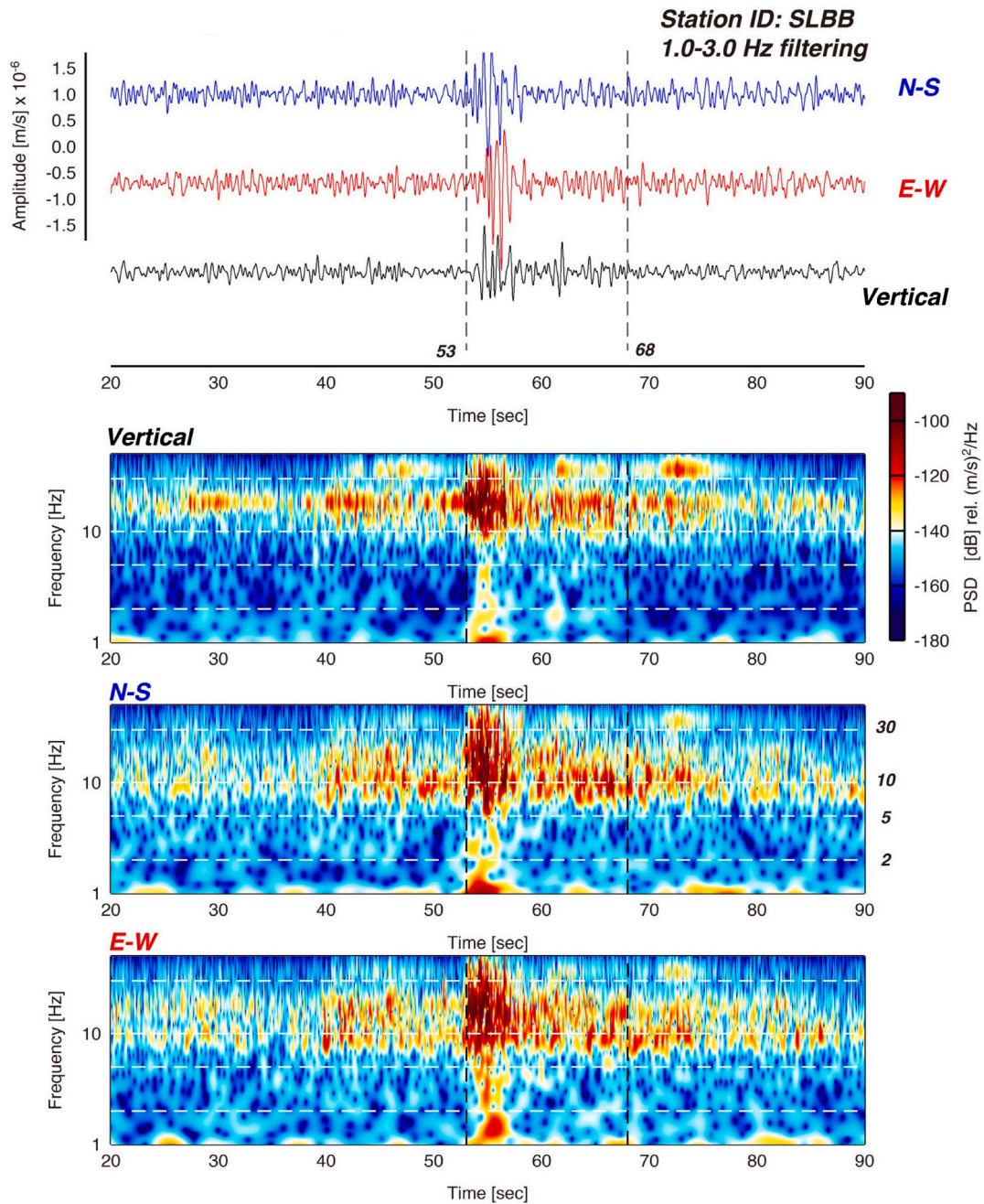


Fig. 10. Results of seismic signal analyses: band-pass filtered (1-3 Hz) three-components seismic records and spectrograms at station SLBB. Colors represent the spectrogram power spectral density (PSD) amplitude in decibels. Vertical dashed lines are starting and ending times of seismic signatures generated by landslide.

located at the end of the middle slope, traveled a distance of approximately 93 m and stopped moving at the forefront of the landslide deposit at the playground. The soil at D5 at the end of the lower slope was first pushed downward by the sliding soil mass and then buried at the bottom of the landslide deposit, resulting in a relatively short travel distance (approximately 15 m), just a few meters away from the retaining wall.

For the rate of landslide movement, the velocity of the soil at D2 gradually increased during the first 9 s until it reached a peak (12.5 m/s), and it then decreased to 0 m/s at the end of the landslide (Fig. 11b). The velocity of the soil at D4 increased rapidly during $t = 4-9$ s due to the accumulation of sliding soil mass during movement from the upper to lower slope. The maximum velocity of the soil at D4 was 13 m/s when the soil was descending from the top of the retaining wall, and the soil reached the playground at approximately $t = 14$ s. The velocity of the soil at D5 suddenly increased and decreased over a short period. These

sudden changes in velocity are attributable to the relatively short travel distance of the soil at D5, as discussed previously. According to the classification system proposed by Cruden and Varnes (1996), the rate of landslide movement of Slope 1 was classified as extremely rapid (>5 m/s).

5.1.3. Post-failure mechanism

Fig. 12 presents the variations in soil volumetric strain and excess PWP with time for the tracking points P1, P2, and P3 at the upper, middle, and lower slope, respectively. The tracking points (Fig. 7a and 9a) were located at the bottom of the residual soil where the soil was subjected to the most intensive shearing. As discussed, the numerical results indicated that the landslide occurred through a complex process of soil failure that involved stages of shearing, translational movement, compression, and deposition. The changes in soil volumetric strain and

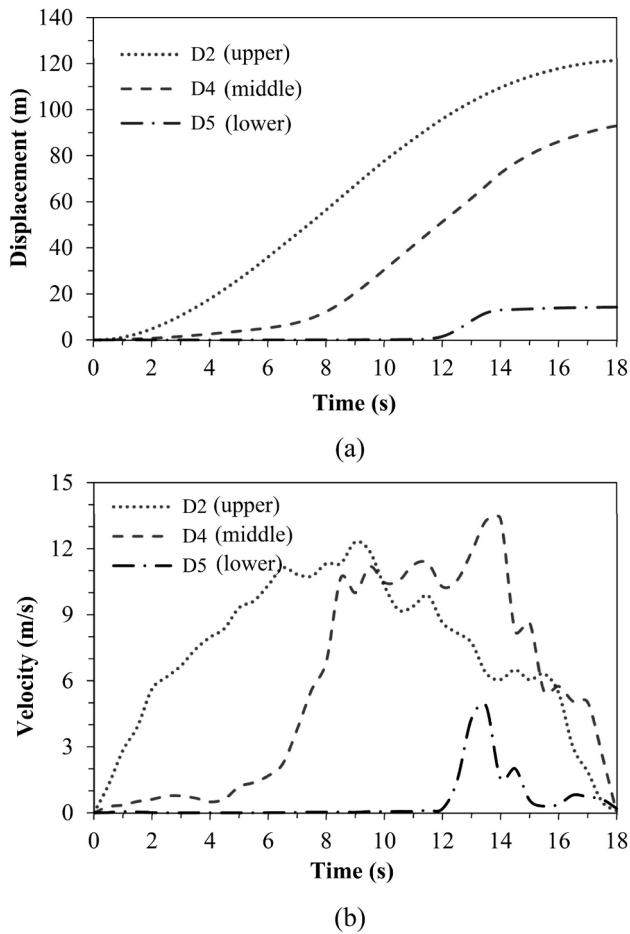


Fig. 11. Kinematic behavior of Slope 1 at different locations: (a) displacement with time; (b) velocity with time.

excess PWP were associated with these stages of failure.

P1 was located at the upper slope, where the soil was mainly subjected to shearing during the landslide (Fig. 9a). At $t = 0-6$ s, the soil at P1 developed positive volumetric strain because it was subjected to compression due to soil resistance from the adjacent soil downhill (Fig. 12a). Corresponding to the development of positive volumetric strain, the soil at P1 generated positive excess PWP as shearing in progress, and a constant positive value was maintained for a few seconds (Fig. 12b). At $t > 6$ s, the soil resistance to the sliding soil mass gradually diminished because the soil located downhill had begun to move (Fig. 9b). Consequently, the volumetric strain of the soil at P1 gradually decreased and became a negative value, indicating that soil transitioned from undergoing compression to undergoing expansion. The excess PWP also decreased correspondingly. The soil at P1 reached a new equilibrium at approximately $t \geq 13$ s, and the soil volumetric strain and excess PWP remained unchanged afterward.

In contrast to the soil at P1, the soil at P2 and P3 consistently developed a positive volumetric strain and excess PWP during the landslide (Fig. 12). P2 was located at the middle slope where the soil was subjected to translational movement and compression (Fig. 9a). The positive volumetric strain and excess PWP of the soil at P2 increased at $t = 6$ s when the soil at the middle slope began to move (Fig. 9b). The volumetric strain and excess PWP reached their maximum values at $t = 9$ s and exhibited fluctuations thereafter due to the successive compression caused by the sliding soil mass followed by expansion caused by the downward movement of the soil.

P3 was located at the lower slope where the soil was subjected to compression and deposition (Fig. 9a). The positive volumetric strain and

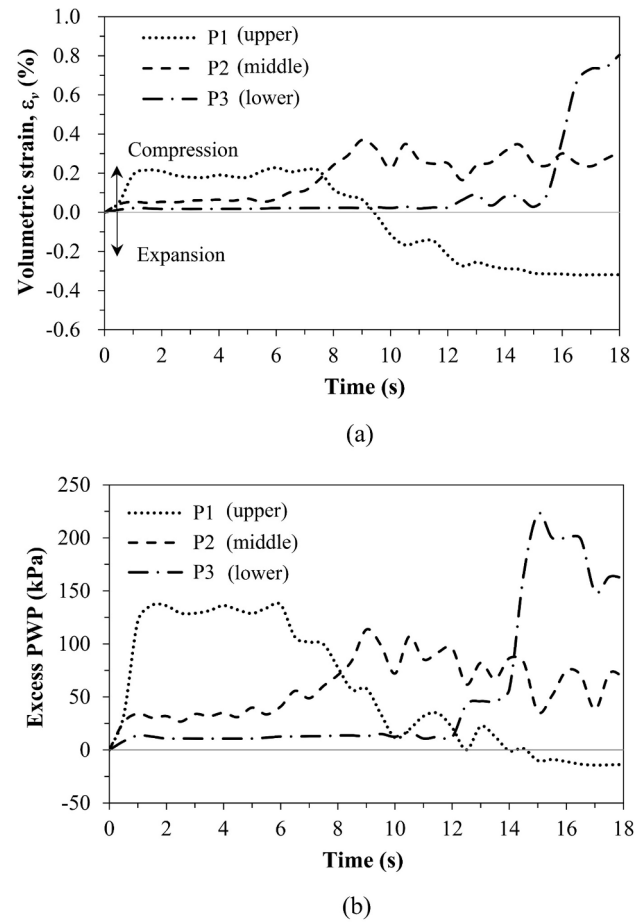


Fig. 12. Post-failure mechanism of Slope 1 at different locations: (a) soil volumetric strain with time; (b) excess porewater pressure with time.

excess PWP of the soil at P3 increased at $t = 12$ s when the sliding soil mass reached the lower slope (Fig. 9b). The volumetric strain and excess PWP values rapidly increased and reached their peaks in a short time due to intensive soil compression driven by the accumulation of sliding soil mass as the soil moved from the upper to lower slope (Fig. 12). After its peak ($t \geq 15$ s), the excess PWP remained at a high value and dissipated slowly until the landslide ultimately stopped. This result is attributable to P3 being buried at the bottom of the landslide deposit and the longer time required for the dissipation of PWP due to the longer drainage path (Fig. 9a).

Notably, high positive excess PWP could develop near the sliding surface, e.g., at P2 and P3, when the soil was subjected to shearing during the landslide. The high positive PWP significantly reduced the soil effective stress, caused a remarkable decrease in soil shear resistance, and thus enhanced the mobility of the soil moving masses. This is the reason why the soil at P3, originally retained by the retaining wall, could climb across the retaining wall to reach the playground. The results also highlight the importance of the influence of excess PWP on the kinematic behavior of landslides. This finding is supported by Conte et al. (2020), who concluded that the excess PWP causing slope failure seems to have the greatest influence on the kinematics of the landslide and consequently on the associated runout distance. Besides, Moriwaki and Sato (1998) and Sassa (1998) also reported that the landslide self-fluidization process, sliding surface liquefaction by the high excess PWP, was the main reason causing the long runout distance of the Hariharagawa landslide.

5.2. Results for Slope 2

5.2.1. Comparison of final landslide profile

Fig. 13 presents a comparison of the final landslide profiles obtained from field observations and numerical predictions. The predicted final landslide profile generally exhibited good agreement with the measured profile. In the landslide deposition area, the predicted runout distance (37.8 m) and deposit height (7.2 m) were similar to the measured values (38 and 7.0 m, respectively) (Table 2). The numerical analysis accurately predicted the deposit height in this case because the presence of the chicken shed prevented the formation of a three-dimensional fan-shaped deposit. The numerical results predicted that the sliding soil mass would bury the chicken shed. Because of the influence of the chicken shed on the kinematics of the landslide, the sliding soil mass did not reach the farmer's house. These numerical results were consistent with the field observations, as described in Section 3.1.

5.2.2. Post-failure process and kinematic behavior

Fig. 14a depicts the development and distribution of the soil deviatoric strain of Slope 2 at different time points. The landslide duration from beginning to end was 14 s. Overall, soil failure occurred retrogressively from the lower to upper slope. At $t = 1$ s, the shear failure surface began to mobilize at the soil-bedrock interface at the toe of the residual soil layer. At $t = 3$ s, the shear failure surface developed, extending to the slope surface. The displacement of the residual soil at

the lower slope could be clearly observed. At $t = 7$ s, as the residual soil at the lower slope moved downward, the residual soil at the upper slope gradually lost support and began to fail actively. The shear failure surface reached to the trailing end of the residual soil at the upper slope. At $t = 10.2$ s, the entire sliding soil mass moved translationally along the soil-bedrock interface and then impacted the chicken shed. In the final stage $t = 11-14$ s, the movement of sliding soil mass was blocked by the chicken shed. The landslide deposit continuously piled up between the toe of the slope and the chicken shed. Finally, at $t = 14$ s, the landslide deposit buried the chicken shed; thereafter, the sliding soil mass completely stopped moving and the kinetic energy rapidly dissipated due to the presence of the structure.

Fig. 14b presents a plot of the horizontal displacement of the soil of Slope 2 at different time points. Fig. 15 displays the variation of the displacement and velocity with time for the three selected tracking points D2, D3, and D5 at the upper, middle, and lower residual soil layers, respectively. The soil at D1, located near the landslide scarp, traveled the shortest distance, with a displacement of only approximately 1.5 m, and stopped sliding at approximately $t = 5$ s. The soil at D2 and D3 (at the upper and middle residual soil layers, respectively) exhibited a displacement of approximately 16.5 and 31.9 m, respectively. The soil at D4 (at the lower residual soil layer) traveled the greatest distance (approximately 45 m) and stopped sliding when it reached the top of the landslide deposit at the toe of the slope. The soil at D5 (at the toe of the residual soil layer) exhibited a displacement of

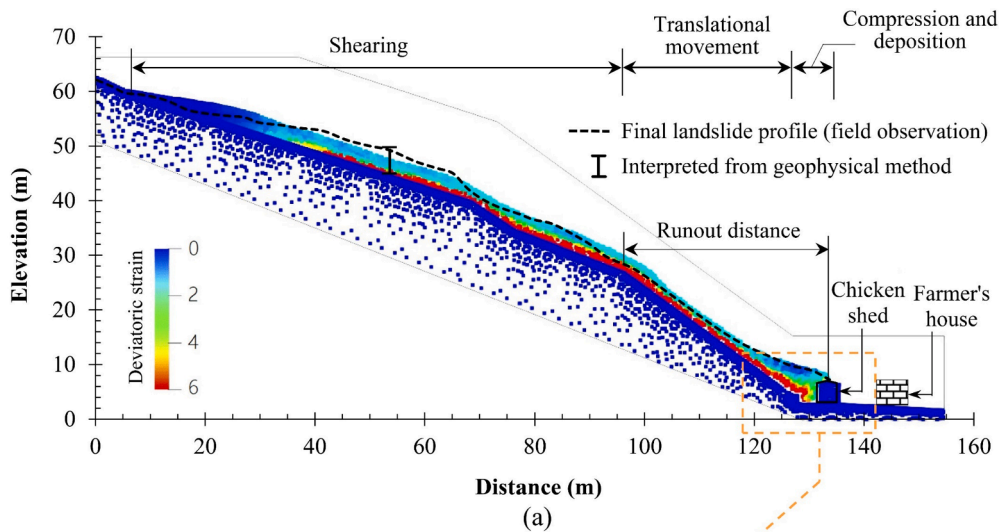


Fig. 13. Model validation: (a) comparison of final landslide profile of Slope 2; (b) photo of landslide reaching to the chicken shed roof.

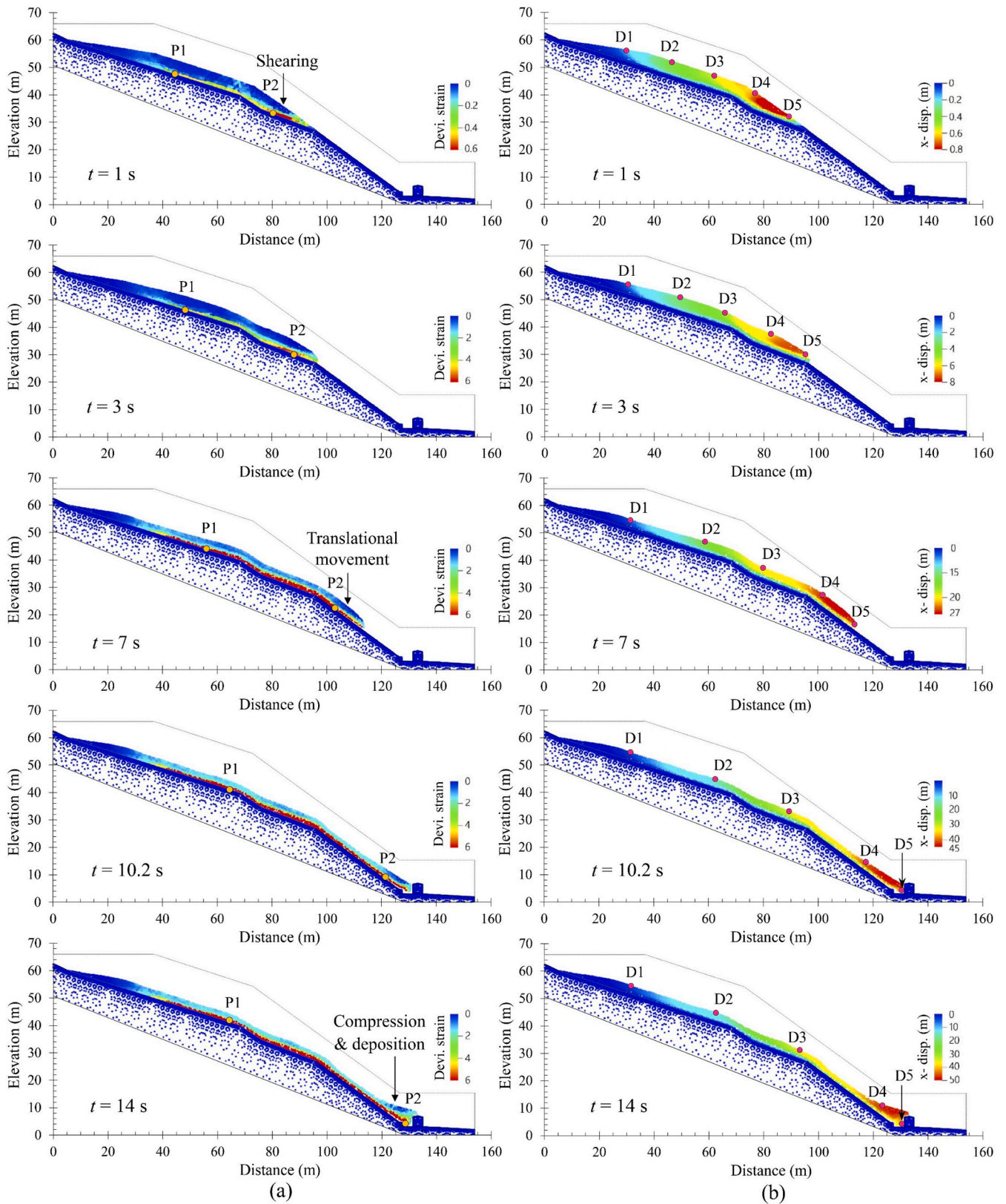


Fig. 14. Post-failure process of Slope 2 at different times: (a) deviatoric strain; (b) horizontal displacement.

approximately 40 m and then stopped sliding when it reached the chicken shed. The soil at D5 was finally buried underneath the landslide deposit due to the accumulation of sliding soil mass.

Regarding the rate of landslide movement, the velocity of the soil at

D2 and D3 gradually increased to its peak (3.0 and 4.4 m/s, respectively) in the first 5 s and then gradually decreased thereafter (Fig. 15b). The velocity of the soil at D5 also exhibited a gradually increasing trend but with two peaks instead of one. The first peak (6 m/s) occurred at $t = 4$ s

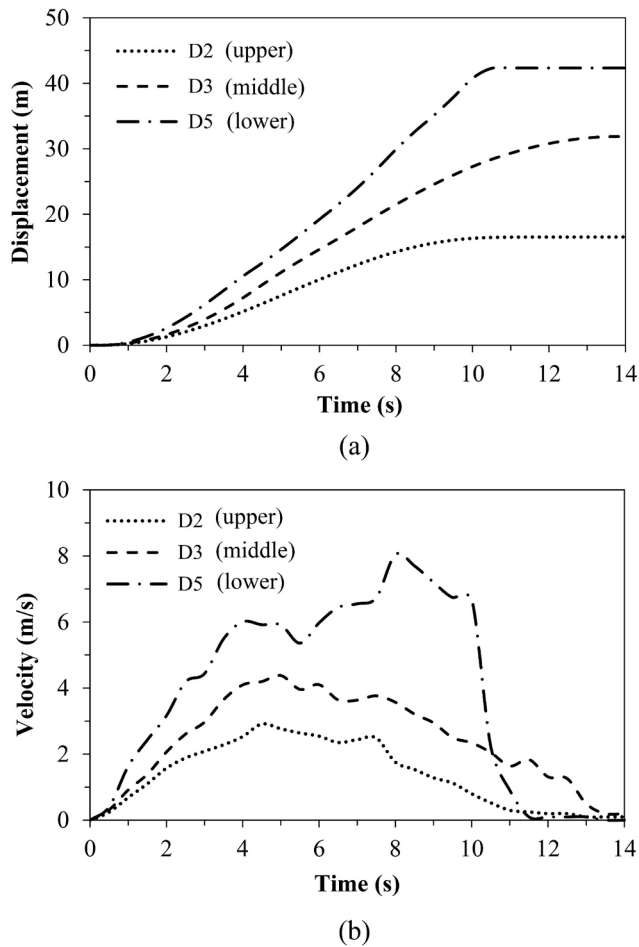


Fig. 15. Kinematic behavior of Slope 2 at different locations: (a) displacement with time; (b) velocity with time.

when the soil at D5 entered the steepest section of the lower slope. The second peak (8 m/s) occurred at $t = 8.5$ s as a result of acceleration due to gravity. The velocity of the soil at D5 rapidly decreased after $t = 10.2$ s and reached 0 m/s at $t = 12$ s as a result of the rapid dissipation of kinetic energy due to the presence of the structure. According to the classification system proposed by Cruden and Varnes (1996), the rate of landslide movement of Slope 2 ranged between very rapid (>5 cm/s) and extremely rapid (>5 m/s).

5.2.3. Post-failure mechanism

Fig. 16 displays the variations in soil volumetric strain and excess PWP over time at the tracking points P1 and P2, which were located at the upper and lower residual soil layers, respectively. P1 was located at the upper slope and was mainly subjected to shearing during the landslide (Fig. 14a). The shearing at P1 caused the development of positive volumetric strain, which correspondingly generated positive excess PWP because of soil compression. At $t = 6$ – 10.2 s, the volumetric strain and excess PWP of the soil at P1 gradually decreased with the decrease in the soil resistance to the sliding soil mass because the lower residual soil layer entered the steepest section of the lower slope with an increasing speed as it moved downhill (Fig. 14b). At $t \geq 10.2$ s, the soil volumetric strain and excess PWP reached constant values as the soil at P1 stopped moving.

P2 was located in the lower residual soil layer where the soil was subjected to shearing, translational movement, compression, and deposition (Fig. 14a). At $t = 0$ – 3 s, the soil at P2 was first subjected to shearing (Fig. 16a). No evident changes in the volumetric strain or excess PWP of the soil at P2 were observed at this time. At $t = 3$ – 9 s, the

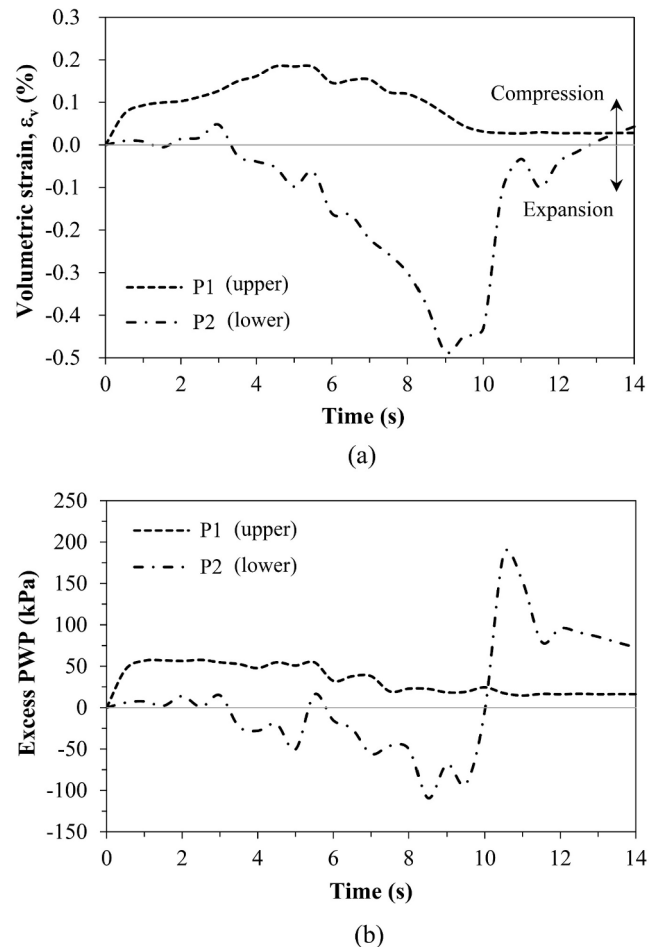


Fig. 16. Post-failure mechanism of Slope 2 at different locations: (a) soil volumetric strain with time; (b) excess porewater pressure with time.

soil at P2 entered the steepest section of the lower slope and underwent translational movement. Because no soil was present at the steepest section of the lower slope to provide resistance for the sliding soil mass, the soil transitioned from a state of compression to a state of expansion. Consequently, the volumetric strain and excess PWP of the soil at P2 gradually decreased and became negative. At approximately $t = 10$ s, the soil at P2 reached the chicken shed and underwent intensive soil compression driven by the accumulation of the sliding soil mass. The volumetric strain and excess PWP rapidly increased again over a short period. The excess PWP increased to a high positive value and did not fully dissipate until the end of the landslide event because the soil at P2 was buried at the bottom of the landslide deposit, which had a longer drainage path for the dissipation of PWP (Fig. 14a).

5.3. Effect of analysis type on landslide kinematics

The durations of the landslides from their beginning to end were only a few seconds (e.g., 18 s for Slope 1 and 14 s for Slope 2). Because landslides generally have a short duration, the loading rate of soil during landslide events is relatively higher than the hydraulic conductivity of the residual soil. Therefore, whether soil modeling can be performed for undrained conditions during a landslide is worth exploring. In this study, two types of analyses (i.e., undrained-effective stress analysis and fully coupled hydro-mechanical analysis) were performed to assess the influence of soil drainage conditions on landslide kinematics. These analyses were conducted using the same soil constitutive model and input soil properties. The sole difference between the two analyses was whether the dissipation of excess PWP was permitted during the

landslide simulation. In the fully coupled analysis, the dissipation of PWP during the landslide was permitted, and the rate of PWP dissipation depended on the hydraulic conductivity of the soil; by contrast, in the undrained analysis, the dissipation of PWP was prohibited to ensure the soil under undrained conditions during the landslide.

Fig. 17 presents a comparison of the final landslide profiles of the two slopes predicted through the two analyses. Table 2 summarizes the results of this comparison. Compared with the fully coupled analysis, the undrained analysis predicted a shorter runout distance and lower deposit height for both landslides. In general, the fully coupled analysis outperformed the undrained analysis in predicting the kinematic behavior of the landslides (Table 2). Compared with the undrained analysis, the fully coupled analysis generally yielded a lower relative error with respect to the field observations. The relative errors for runout distance and deposit height predictions were respectively +10.8% and +39.0% for Slope 1 and +0.5% and +4.7% for Slope 2 in the fully coupled analysis, and -20.5% and +32.9% for Slope 1 and -6.8% and -32.9% for Slope 2 in the undrained analysis. In landslide risk assessment, underestimate of the runout distance in undrained analysis may lead to unconservative results to assess the landslide impact area. Notably, although the fully coupled analysis produced a more accurate prediction of landslide kinematic behavior and could adequately simulate changes in PWP during landslides, its computational time was

significantly more than that of the undrained analysis. As indicated in Table 2, the computational time of the fully coupled analysis was approximately 4–6 days, whereas that of the undrained analysis was less than 1 h.

Figs. 18 and 19 display the excess PWP distributions for the two types of analyses at different time points for Slopes 1 and 2, respectively. These distributions were compared to understand the reason for the difference between the two analysis approaches in terms of the predicted results for landslide kinematic behavior. As indicated in Figs. 18 and 19, the undrained analysis generated more negative excess PWP (MPs with red and yellow points) than the fully coupled analysis, especially at the slope surface. These negative excess PWP values generated during the undrained analysis could not increase to positive values because PWP dissipation was prohibited during the landslide simulation; this resulted in increases in soil effective stress and shear strength and thus a decrease in landslide mobility (i.e., shorter runout distance and lower deposit height). By contrast, the fully coupled analysis could appropriately simulate the changes in PWP during the landslide. Fewer negative excess PWP values were generated in the fully coupled analysis because the dissipation of PWP was permitted, resulting in a more accurate prediction of landslide kinematic behavior in the post-failure stage. This finding is consistent with that of van Asch et al. (2007), who highlighted the role of rapid changes in soil stress and PWP in controlling landslide

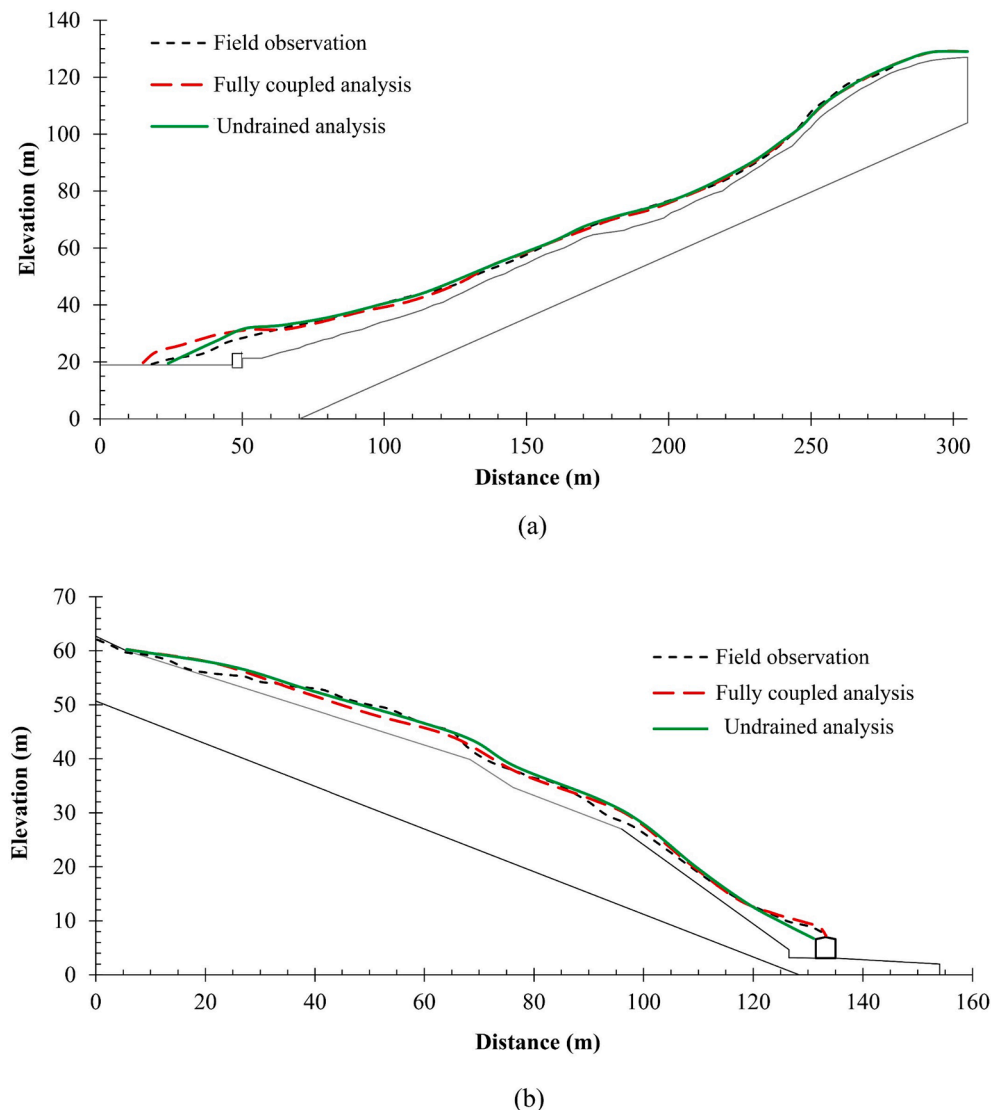


Fig. 17. Comparison of the final landslide profile predicted by different types of analyses: (a) Slope 1; (b) Slope 2.

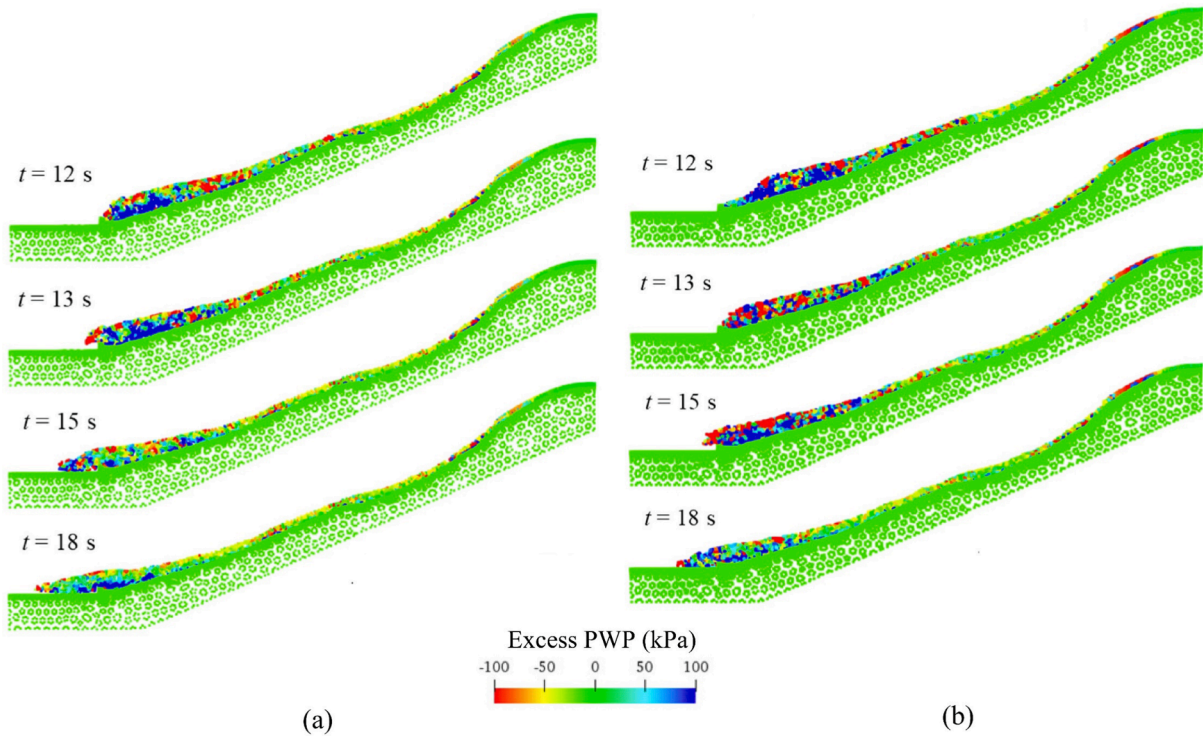


Fig. 18. Excess porewater pressure distribution within Slope 1 at different times: (a) fully coupled analysis; (b) undrained analysis.

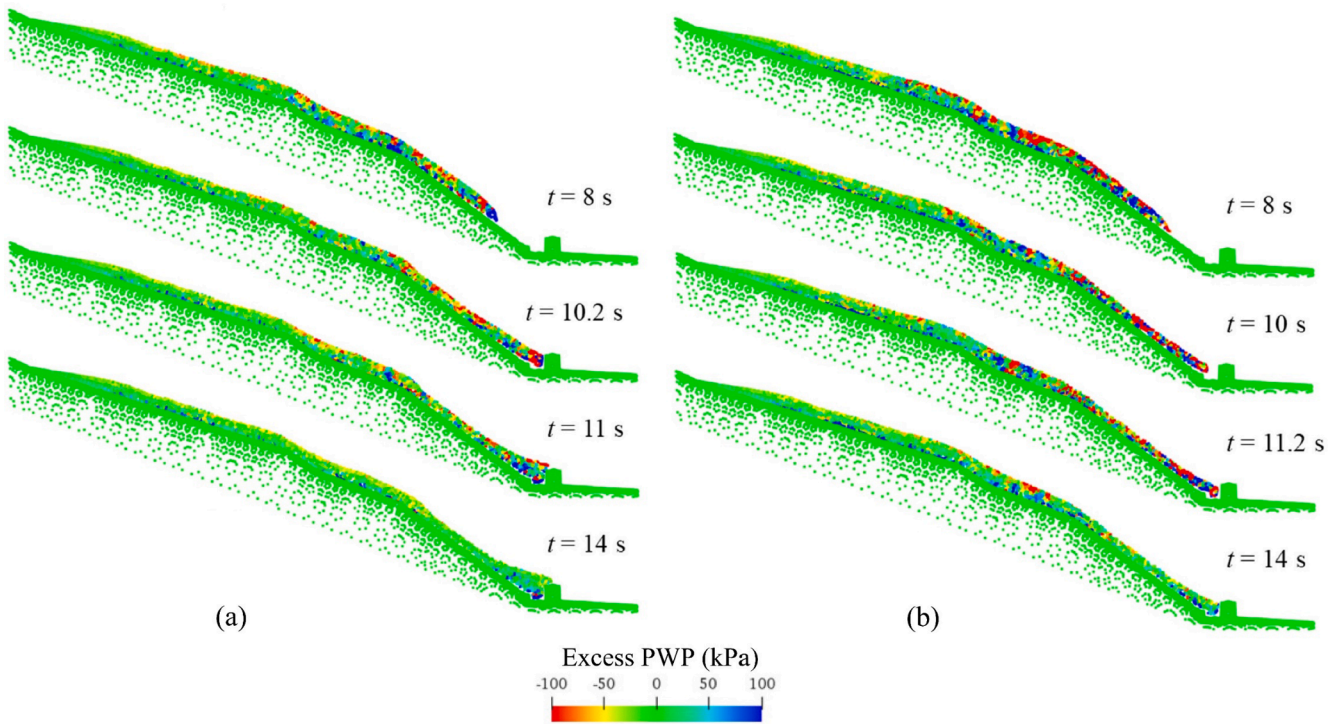


Fig. 19. Excess porewater pressure distribution within Slope 2 at different times: (a) fully coupled analysis; (b) undrained analysis.

mobility.

6. Conclusions

This paper presents a comprehensive and well-documented landslide case study involving detailed site investigation, field tests, seismic signal

analyses, and advanced numerical analyses using the material point method to investigate the post-failure process and kinematic behavior of two landslides. The numerical results were examined to understand the post-failure process and mechanism of the landslides. Moreover, the effects of soil drainage conditions during landslides on the final landslide profile were also compared. The following main conclusions can be

drawn:

- The MPM was demonstrated to be a suitable and applicable numerical tool for analyzing landslide kinematics during post-failure stages. Two-dimensional MPM analyses yielded accurate predictions of the runout distance of both landslides; however, two-dimensional MPM analyses underestimated the deposit height as a result of the inability to account for three-dimensional topographic effects (i.e., fan-shaped deposit) in the field.
- The landslides occurred through a complex process of soil failure involving stages of shearing, translational movement, compression, and deposition. The soil was subjected to different loading conditions in different stages, and the corresponding post-failure mechanisms (i.e., variations in deviatoric strain, volumetric strain, and excess PWP over time) were also different.
- The post-failure process of Slope 1 occurred progressively from the upper to lower slope. The slip failure was the soil–bedrock interface of the upper slope. The sliding soil mass at the upper slope moved downward, compressing and pushing the soil downhill to cause passive failure. Finally, the sliding soil mass completely stopped and was deposited in the playground area when the kinetic energy had fully dissipated through friction and shear deformation.
- The post-failure process of Slope 2 occurred retrogressively from the lower to upper slope. The shear failure surface began to mobilize at the soil–bedrock interface at the toe of the residual soil layer. As the residual soil at the lower slope moved downward, the residual soil at the upper slope gradually lost support and underwent active failure. The sliding soil mass reached and impacted the chicken shed. Finally, the landslide deposit buried the chicken shed; the sliding soil mass completely stopped moving as its kinetic energy rapidly dissipated as a result of the presence of the structure.
- The generation of excess PWP during landslides has a significant influence on landslide kinematics and final landslide profiles. High positive excess PWP could develop near the sliding surface when the soil was subjected to shearing during the landslide. The high positive PWP significantly reduced the soil effective stress, caused a remarkable decrease in soil shear resistance, and thus enhanced the mobility of the soil moving masses.
- The fully coupled analysis outperformed the undrained analysis in predicting landslide kinematics. The undrained analysis generated more negative excess PWP than the fully coupled analysis, especially at the slope surface, resulting in an increase in soil effective stress and shear strength and thus a decrease in landslide mobility. By contrast, the fully coupled analysis permitted the dissipation of PWP, resulting in a more accurate prediction of landslide kinematics in the post-failure stage. However, the computational time of the fully coupled analysis was significantly more than that of the undrained analysis.

CRedit authorship contribution statement

Thanh Son Nguyen: Software, Formal analysis, Data curation, Writing – original draft, Funding acquisition. **Kuo-Hsin Yang:** Conceptualization, Methodology, Investigation, Writing – original draft, Supervision, Project administration, Funding acquisition. **Yu-Kuei Wu:** Software, Formal analysis, Data curation, Visualization. **Fuchen Teng:** Conceptualization. **Wei-An Chao:** Formal analysis, Data curation. **Wei-Lin Lee:** Conceptualization.

Declaration of Competing Interest

The authors declare that they have no known competing financial interests or personal relationships that could have appeared to influence the work reported in this paper.

Acknowledgments

The research work is funded by Hanoi University of Civil Engineering (HUCE), Viet Nam under Grant number 18-2021/KHXD-TĐ and supported by the Ministry of Science and Technology, Taiwan under Grant No. MOST 107-2628-E-002-003-MY3. The financial supports are gratefully acknowledged. The authors sincerely appreciate the Taiwan Professional Geotechnical Engineers Association for providing the site investigation information for the case studies in this paper. The authors also sincerely appreciate Mr. Chao-Wei Chen, the general manager in Land Engineering Consultants, and Mr. Ren-Da Chen, the general manager in the Artech Engineering Service, for providing and discussing the details of landslide investigation of the cases studies.

References

- Andersen, S., Andersen, L., 2010. Modelling of landslides with the material-point method. *Comput. Geosci.* 14 (1), 137–147.
- Anura3D_v2019. MPM Research Community. Available online: <http://www.anura3d.com>.
- Bandara, S., Ferrari, A., Laloui, L., 2016. Modelling landslides in unsaturated slopes subjected to rainfall infiltration using material point method. *Int. J. Numer. Analyt. Methods Geomech.* 40 (9), 1358–1380.
- Bandara, S., Soga, K., 2015. Coupling of soil deformation and pore fluid flow using material point method. *Comput. Geotech.* 63, 199–214.
- Bui, H.H., Fukagawa, R., Sako, K., Ohno, S., 2008. Lagrangian meshfree particles method (SPH) for large deformation and failure flows of geomaterial using elastic-plastic soil constitutive model. *Int. J. Numer. Analyt. Methods Geomech.* 32 (12), 1537–1570.
- Ceccato, F., Yerro, A., Girardi, V., Simonini, P., 2021. Two-phase dynamic MPM formulation for unsaturated soil. *Comput. Geotech.* 129, 103876. <https://doi.org/10.1016/j.compgeo.2020.103876>.
- Chang, J.-M., Chao, W.-A., Chen, H., Kuo, Y.-T., Yang, C.-M., 2021. Locating rock slope failures along highways and understanding their physical processes using seismic signals. *Earth Surf. Dyn.* 9 (3), 505–517.
- Chang, Z., Huang, F., Huang, J., Jiang, S.-H., Zhou, C., Zhu, L., 2020. Experimental study of the failure mode and mechanism of loess fill slopes induced by rainfall. *Eng. Geol.* 105941.
- Chen, C.-H., Chao, W.-A., Wu, Y.-M., Zhao, L.-i., Chen, Y.-G., Ho, W.-Y., Lin, T.-L., Kuo, K.-H., Chang, J.-M., 2013. A seismological study of landquakes using a real-time broadband seismic network. *Geophys. J. Int.* 194 (2), 885–898.
- Chen, K.-T., Wu, J.-H., 2018. Simulating the failure process of the Xinmo landslide using discontinuous deformation analysis. *Eng. Geol.* 239, 269–281.
- Chen, Q., Fan, G., Zhou, J.-W., 2020. Numerical simulation of the 2017 Xinmo catastrophic landslide considering entrainment effect. *Front. Earth Sci.* 8.
- Chen, W., Qiu, T., 2012. Numerical simulations for large deformation of granular materials using smoothed particle hydrodynamics method. *Int. J. Geomech.* 12 (2), 127–135.
- Cogan, J., Gratchev, I., 2019. A study on the effect of rainfall and slope characteristics on landslide initiation by means of flume tests. *Landslides* 16 (12), 2369–2379.
- Conte, E., Pugliese, L., Troncone, A., 2019. Post-failure stage simulation of a landslide using the material point method. *Eng. Geol.* 253, 149–159.
- Conte, E., Pugliese, L., Troncone, A., 2020. Post-failure analysis of the Maierato landslide using the material point method. *Eng. Geol.* 277, 105788. <https://doi.org/10.1016/j.enggeo.2020.105788>.
- Cruden, D.M., Varnes, D.J., 1996. Landslide types and processes. Special Report - National Research Council, Transportation Research Board 247, 36–75.
- Cuomo, S., Di Perna, A., Martinelli, M., 2021. Modelling the spatio-temporal evolution of a rainfall-induced retrogressive landslide in an unsaturated slope. *Eng. Geol.* 294, 106371. <https://doi.org/10.1016/j.enggeo.2021.106371>.
- Dai, Z., Wang, F., Yang, H., Qin, S., 2020. Numerical investigation on the kinetic characteristics of the Yigong landslide in Tibet, China. *Nat. Hazards Earth Syst. Sci.* 2020, 1–25.
- Fan, W., Wei, Y.-n., Deng, L., 2018. Failure modes and mechanisms of shallow debris landslides using an artificial rainfall model experiment on Qin-ba mountain. *Int. J. Geomech.* 18 (3), 04017157. [https://doi.org/10.1061/\(ASCE\)GM.1943-5622.0001068](https://doi.org/10.1061/(ASCE)GM.1943-5622.0001068).
- Feng, K., Huang, D., Wang, G., 2021. Two-layer material point method for modeling soil–water interaction in unsaturated soils and rainfall-induced slope failure. *Acta Geotech.* 16 (8), 2529–2551.
- Fern, E., Rohe, A., Soga, K., Alonso, E., 2019. The material point method for geotechnical engineering: A practical guide, first ed. CRC Press.
- Girardi, V., Yerro, A., Ceccato, F., Simonini, P., 2021. Modelling deformations in water retention structures with unsaturated material point method. *Proc. Inst. Civ. Eng. Geotech. Eng.* 174 (5), 577–592.
- Goodman, R.E., 1989. Introduction to Rock Mechanics, second ed. Wiley.
- Guo, J., Yi, S., Yin, Y., Cui, Y., Qin, M., Li, T., Wang, C., 2020. The effect of topography on landslide kinematics: a case study of the Jichang town landslide in Guizhou, China. *Landslides* 17 (4), 959–973.
- Harrison, J.F., Chang, C.H., 2019. Sustainable management of a mountain community vulnerable to geohazards: a case study of maolin district, Taiwan. *Sustainability* 11 (15), 4107.

- Huang, Y.u., Dai, Z., 2014. Large deformation and failure simulations for geo-disasters using smoothed particle hydrodynamics method. *Eng. Geol.* 168, 86–97.
- Hung, C., Liu, C.-H., Chang, C.-M., 2018. Numerical investigation of rainfall-induced landslides in mudstone using coupled finite and discrete element analysis. *Geofluids* 2018, 1–15.
- Kulhawy, F.H., Mayne, P.W., 1990. Manual on Estimating Soil Properties for Foundation Design. Electric Power Research Institute, Palo Alto, California.
- Lee, K., Suk, J., Kim, H., Jeong, S., 2021a. Modeling of rainfall-induced landslides using a full-scale flume test. *Landslides* 18 (3), 1153–1162.
- Lee, W.-L., Martinelli, M., Shieh, C.-L., 2021b. An investigation of rainfall-induced landslides from the pre-failure stage to the post-failure stage using the Material Point Method. *Front. Earth Sci.* 9 <https://doi.org/10.3389/feart.2021.764393>.
- Leshchinsky, B., Vahedifard, F., Koo, H.-B., Kim, S.-H., 2015. Yumokjeong landslide: an investigation of progressive failure of a hillslope using the finite element method. *Landslides* 12 (5), 997–1005.
- Li, L., Wang, Y.u., Zhang, L., Choi, C., Ng, C.W.W., 2019. Evaluation of critical slip surface in limit equilibrium analysis of slope stability by Smoothed Particle Hydrodynamics. *Int. J. Geomech.* 19 (5), 04019032. [https://doi.org/10.1061/\(ASCE\)GM.1943-5622.0001391](https://doi.org/10.1061/(ASCE)GM.1943-5622.0001391).
- Li, W.C., Dai, F.C., Wei, Y.Q., Wang, M.L., Min, H., Lee, L.M., 2016a. Implication of subsurface flow on rainfall-induced landslide: a case study. *Landslides* 13 (5), 1109–1123.
- Li, W.C., Li, H.J., Dai, F.C., Lee, L.M., 2012. Discrete element modeling of a rainfall-induced flowslide. *Eng. Geol.* 149–150, 22–34.
- Li, X., Tang, X., Zhao, S., Yan, Q., Wu, Y., 2021. MPM evaluation of the dynamic runout process of the giant Daguangbao landslide. *Landslides* 18 (4), 1509–1518.
- Li, X., Wu, Y., He, S., Su, L., 2016b. Application of the material point method to simulate the post-failure runout processes of the Wangjiayan landslide. *Eng. Geol.* 212, 1–9.
- Lin, C.-W., Chang, W.-S., Liu, S.-H., Tsai, T.-T., Lee, S.-P., Tsang, Y.-C., Shieh, C.-L., Tseng, C.-M., 2011. Landslides triggered by the 7 August 2009 Typhoon Morakot in southern Taiwan. *Eng. Geol.* 123 (1–2), 3–12.
- Lin, D., Hung, S.-H., Liu, W., Chou, J.-C., 2018. Evaluating the efficiency of stability remediation measures for the T16-Tower pier slope of the Taipei Maokong tramway. *J. Mar. Sci. Technol.* 26, 352–373.
- Lin, H.-D., Huang, J.-R., Wang, W.-C., Chen, C.-W., 2019. Study of an unsaturated slope failure due to rainfall infiltration in Wenshan district of Taipei city. *J. GeoEng.* 14 (4), 277–289.
- Liu, C., Yu, Z., Zhao, S., 2021. A coupled SPH-DEM-FEM model for fluid-particle-structure interaction and a case study of Wenjia gully debris flow impact estimation. *Landslides* 18 (7), 2403–2425.
- Liu, X., Wang, Y.u., 2021. Probabilistic simulation of entire process of rainfall-induced landslides using random finite element and material point methods with hydro-mechanical coupling. *Comput. Geotech.* 132, 103989. <https://doi.org/10.1016/j.compegeo.2020.103989>.
- Liu, X., Wang, Y.u., Li, D.-Q., 2020. Numerical simulation of the 1995 rainfall-induced Fei Tsui Road landslide in Hong Kong: new insights from hydro-mechanically coupled material point method. *Landslides* 17 (12), 2755–2775.
- Llano-Serna, M.A., Farias, M.M., Pedrosa, D.M., 2016. An assessment of the material point method for modelling large scale run-out processes in landslides. *Landslides* 13 (5), 1057–1066.
- Lollino, P., Giordan, D., Allasia, P., 2016. Assessment of the behavior of an active earth-slope by means of calibration between numerical analysis and field monitoring. *Bull. Eng. Geol. Environ.* 76 (2), 421–435.
- Lu, C.-Y., Tang, C.-L., Chan, Y.-C., Hu, J.-C., Chi, C.-C., 2014. Forecasting landslide hazard by the 3D discrete element method: A case study of the unstable slope in the Lushan hot spring district, central Taiwan. *Eng. Geol.* 183, 14–30.
- Mohammadi, S., Taiebat, H., 2016. Finite element simulation of an excavation-triggered landslide using large deformation theory. *Eng. Geol.* 205, 62–72.
- Mori, H., Chen, X., Leung, Y.F., Shimokawa, D., Lo, M.K., 2020. Landslide hazard assessment by smoothed particle hydrodynamics with spatially variable soil properties and statistical rainfall distribution. *Can. Geotech. J.* 57 (12), 1953–1969.
- Moriwaki, H., Inokuchi, T., Hattajji, T., Sassa, K., Ochiai, H., Wang, G., 2004. Failure processes in a full-scale landslide experiment using a rainfall simulator. *Landslides* 1 (4), 277–288.
- Moriwaki, H., Sato, T., 1998. Motion and fluidization of a Hariharagawa landslide, south Japan. Proceedings of International Union of Forest Research Organization Conference, Environmental Forest Science.
- Nian, T.-K., Zhang, Y.-J., Wu, H., Chen, G.-q., Zheng, L.u., 2020. Runout simulation of seismic landslides using discontinuous deformation analysis (DDA) with state-dependent shear strength model. *Can. Geotech. J.* 57 (8), 1183–1196.
- Nonoyama, H., Moriguchi, S., Sawada, K., Yashima, A., 2015. Slope stability analysis using smoothed particle hydrodynamics (SPH) method. *Soils Found.* 55 (2), 458–470.
- Nguyen, T.S., Yang, K.-H., Ho, C.-C., Huang, F.-C., Toth, T.M., 2021. Postfailure characterization of shallow landslides using the material point method. *Geofluids* 2021, 1–25.
- Ochiai, H., Okada, Y., Furuya, G., Okura, Y., Matsui, T., Sammori, T., Terajima, T., Sassa, K., 2004. A fluidized landslide on a natural slope by artificial rainfall. *Landslides* 1 (3), 211–219.
- Peng, W., Song, S.Y., Yu, C.J., Bao, Y.D., Sui, J.X., Hu, Y., 2019. Forecasting landslides via three-dimensional discrete element modeling: Helong landslide case study. *Appl. Sci.* 9 (23), 5242.
- Petley, D., 2012. Global patterns of loss of life from landslides. *Geology* 40 (10), 927–930.
- Picarelli, L., Urciuoli, G., Ramondini, M., Comegna, L., 2005. Main features of mudslides in tectonised highly fissured clay shales. *Landslides* 2 (1), 15–30.
- Qin, J., Mei, G., Xu, N., 2022. Meshfree methods in geohazards prevention: A survey. *Arch. Comput. Methods Eng.* <https://doi.org/10.1007/s11831-021-09686-4>.
- Ren, Y., Li, T., Dong, S., Tang, J., Xue, D., 2020. Rainfall-induced reactivation mechanism of a landslide with multiple-soft layers. *Landslides* 17 (5), 1269–1281.
- Sassa, K., 1998. Mechanisms of landslide-triggered debris flows. In: Keynote Lecture for the IUFRO (International Union of Forestry Research Organization) Division Conference, Environmental Forest Science, vol. 54. Forestry Science, Kluwer, Dordrecht, pp. 499–518.
- Sasahara, K., 2017. Prediction of the shear deformation of a sandy model slope generated by rainfall based on the monitoring of the shear strain and the pore pressure in the slope. *Eng. Geol.* 224, 75–86.
- Schmertmann, J.H., 1970. Static cone to compute static settlement over sand. *J. Soil Mech. Found. Div. ASCE* 96 (3), 1011–1043.
- Shi, J.-J., Zhang, W., Wang, B., Li, C.-Y., Pan, B.o., 2020. Simulation of a submarine landslide using the coupled material point method. *Math. Problems Eng.* 2020, 1–14.
- Shi, B., Zhang, Y., Zhang, W., 2019. Run-out of the 2015 Shenzhen landslide using the material point method with the softening model. *Bull. Eng. Geol. Environ.* 78 (2), 1225–1236.
- Shi, B., Zhang, Y., Zhang, W., 2018. Analysis of the entire failure process of the rotational slide using the material point method. *Int. J. Geomech.* 18 (8), 04018092. [https://doi.org/10.1061/\(ASCE\)GM.1943-5622.0001211](https://doi.org/10.1061/(ASCE)GM.1943-5622.0001211).
- Soga, K., Alonso, E., Yerro, A., Kumar, K., Bandara, S., 2016. Trends in large-deformation analysis of landslide mass movements with particular emphasis on the material point method. *Geotechnique* 66 (3), 248–273.
- Tang, Y., Wu, W., Yin, K., Wang, S., Lei, G., 2019. A hydro-mechanical coupled analysis of rainfall induced landslide using a hypoplastic constitutive model. *Comput. Geotech.* 112, 284–292.
- Troncone, A., Pugliese, L., Conte, E., 2022. Analysis of an excavation-induced landslide in stiff clay using the material point method. *Eng. Geol.* 296, 106479. <https://doi.org/10.1016/j.enggeo.2021.106479>.
- Troncone, A., Pugliese, L., Conte, E., 2020. Run-out simulation of a landslide triggered by an increase in the groundwater level using the material point method. *Water* 12 (10), 2817.
- Troncone, A., Conte, E., Pugliese, L., 2019. Analysis of the slope response to an increase in pore water pressure using the material point method. *Water* 11 (7), 1446.
- Tsou, C.-Y., Feng, Z.-Y., Chigira, M., 2011. Catastrophic landslide induced by Typhoon Morakot, ShiaoLin, Taiwan. *Geomorphology* 127 (3–4), 166–178.
- Tu, X.B., Kwong, A.K.L., Dai, F.C., Tham, L.G., Min, H., 2009. Field monitoring of rainfall infiltration in a loess slope and analysis of failure mechanism of rainfall-induced landslides. *Eng. Geol.* 105 (1–2), 134–150.
- van Asch, T.W.J., Van Beek, L.P.H., Bogaard, T.A., 2007. Problems in predicting the mobility of slow-moving landslides. *Eng. Geol.* 91 (1), 46–55.
- Vanapalli, S.K., Fredlund, D.G., Pufahl, D.E., Clifton, A.W., 1996. Model for the prediction of shear strength with respect to soil suction. *Can. Geotech. J.* 33 (3), 379–392.
- Wang, B., Vardon, P.J., Hicks, M.A., 2016. Investigation of retrogressive and progressive slope failure mechanisms using the material point method. *Comput. Geotech.* 78, 88–98.
- Wang, B., Vardon, P.J., Hicks, M.A., 2018. Rainfall-induced slope collapse with coupled material point method. *Eng. Geol.* 239, 1–12.
- Weng, M.-C., Lin, M.-L., Lo, C.-M., Lin, H.-H., Lin, C.-H., Lu, J.-H., Tsai, S.-J., 2019. Evaluating failure mechanisms of dip slope using a multiscale investigation and discrete element modelling. *Eng. Geol.* 263, 105303. <https://doi.org/10.1016/j.enggeo.2019.105303>.
- Xie, J., Uchimura, T., Wang, G., Selvarajah, H., Maqsood, Z., Shen, Q., Mei, G., Qiao, S., 2020. Predicting the sliding behavior of rotational landslides based on the tilting measurement of the slope surface. *Eng. Geol.* 269, 105554. <https://doi.org/10.1016/j.enggeo.2020.105554>.
- Xu, X., Jin, F., Sun, Q., Soga, K., Zhou, G.G.D., 2019. Three-dimensional material point method modeling of runout behavior of the Hongshiyuan landslide. *Can. Geotech. J.* 56 (9), 1318–1337.
- Yang, K.-H., Nguyen, T.S., Rahardjo, H., Lin, D.-G., 2020. Deformation characteristics of unstable shallow slopes triggered by rainfall infiltration. *Bull. Eng. Geol. Environ.* 80 (1), 317–344.
- Yang, K.-H., Uzuoka, R., Thuo, J.N., Lin, G.-L., Nakai, Y., 2017. Coupled hydro-mechanical analysis of two unstable unsaturated slopes subject to rainfall infiltration. *Eng. Geol.* 216, 13–30.
- Yerro, A., Alonso, E.E., Pinyol, N.M., 2016. Run-out of landslides in brittle soils. *Comput. Geotech.* 80, 427–439.
- Yerro, A., Girardi, V., Martinelli, M., Ceccato, F., 2022. Modelling unsaturated soils with the Material Point Method. A discussion of the state-of-the-art. *Geomech. Energy Environ.* 100343. <https://doi.org/10.1016/j.gete.2022.100343>.
- Yerro, A., Soga, K., Bray, J., 2019. Runout evaluation of Oso landslide with the material point method. *Can. Geotech. J.* 56 (9), 1304–1317.
- Ying, C., Zhang, K., Wang, Z.-N., Siddiqua, S., Makeen, G.M.H., Wang, L., 2021. Analysis of the run-out processes of the Xinlu Village landslide using the generalized interpolation material point method. *Landslides* 18 (4), 1519–1529.
- Yu, F.-C., Chen, T.-C., Lin, M.-L., Chen, C.-Y., Yu, W.-H., 2006. Landslides and rainfall characteristics analysis in Taipei City during the Typhoon Nari event. *Nat. Hazards* 37 (1–2), 153–167.
- Yuan, W.-H., Liu, K., Zhang, W., Dai, B., Wang, Y., 2020. Dynamic modeling of large deformation slope failure using smoothed particle finite element method. *Landslides* 17 (7), 1591–1603.
- Zhang, F., Yashima, A., Osaki, H., Adachi, T., Oka, F., 2003. Numerical simulation of progressive failure in cut slope of soft rock using a soil-water coupled finite element analysis. *Soils Found.* 43 (5), 119–131.

- Zhang, W., Ji, J., Gao, Y., 2020. SPH-based analysis of the post-failure flow behavior for soft and hard interbedded earth slope. *Eng. Geol.* 267, 105446. <https://doi.org/10.1016/j.enggeo.2019.105446>.
- Zhang, X., Wang, L., Krabbenhoft, K., Tinti, S., 2019a. A case study and implication: particle finite element modelling of the 2010 Saint-Jude sensitive clay landslide. *Landslides* 17, 117–1127.
- Zhang, Z., Jin, X., Bi, J., 2019b. Development of an SPH-based method to simulate the progressive failure of cohesive soil slope. *Environ. Earth Sci.* 78 (17), 537.
- Zhao, S., He, S., Li, X., Deng, Y.u., Liu, Y., Yan, S., Bai, X., Xie, Y., 2021. The Xinmo rockslide-debris avalanche: An analysis based on the three-dimensional material point method. *Eng. Geol.* 287, 106109. <https://doi.org/10.1016/j.enggeo.2021.106109>.
- Zhu, L., Deng, Y.u., He, S., 2019. Characteristics and failure mechanism of the 2018 Yanyuan landslide in Sichuan, China. *Landslides* 16 (12), 2433–2444.